UNIVERSITY OF MANCHESTER
School of Electrical and Electronic Engineering
Sackville Street Building
Manchester M60 1QD

DESIGN STUDY ANNUAL REPORT

Yongwei Zhang, Maksims Abalenkovs, Christos Argyropoulos,
Fumie Costen, Anthony Brown

Progress Report

September 5, 2007

Abstract

This design study annual report for the SKADS project covers (i) various antenna array architectures and their specific properties, (ii) potential for the antenna array simulation on high performance systems using the FDTD method and (iii) calculation of the input impedance value by post-processing the FDTD data.

Potential antenna elements for use in a close-packed phased array are investigated. The stripline-fed tapered slot antenna array is studied first as it has potential for wide-band operation with wide scan angles. A new slotline taper profile and variations of radiation plate architectures are investigated to seek the optimum scan performance.

Bunny ear type of antennas is designed to provide low cross-pol and low-profile characteristics with flared dipole structure. It can provide close-to-linear polarisation radiation in the principle planes. However, a balanced feeding scheme for this antenna is preferred, although a successful coaxial cable feeding scheme has been reported.

Munk dipole antenna arrays or slot element arrays are competitive candidates for wide scan angle applications. Layers of dielectric material are needed to keep impedance stability over wide scan angles. A matching section is required to obtain the broad bandwidth a Munk antenna can offer. The impedance curve on the Smith chart is positioned therefore a matching section can be designed in the feed point to produce an acceptable VSWR performance.

A single element rolling a metal strip profile into taper slot structure is engineered. The intention is to design an economical element to form an array with element spacing of one-half wavelength at the lowest frequency. Grating lobes processing for higher frequency is to be done with prior information of their characteristics.

Starting with the description of high performance systems and discussing current research successes and failures a detailed analysis of the potential performance of the supercomputers will be made. Theoretical estimation of maximum amount of antenna elements feasible for efficient simulation is supported by the practical data gained through a series of experiments.

An approach for measuring an input impedance from the FDTD simulation data was developed. The rectangular coaxial cable characteristic impedance in the FDTD scheme was calculated as an example.

Table of Contents

List of Figures

List of Tables

Chapter 1

Phased Array Antenna Design

1.1 Tapered Slot Aperture Antenna

1.1.1 Introduction

The tapered slot antenna (TSA) array was first introduced in 1974 by Lewis et al. [LFH74]. It can operate over wide-band in phased arrays that scan over wide angles. It has been indicated in [YKK$^+$84] that single antennas works best when the length of slot-line is over one wavelength long and the width of the aperture is more than one-half wavelength. However, the antenna element in an array is much smaller than the isolated antenna in order to avoid grating lobes. For instance, 45 degree scan at 1 GHz require the element spacing is less than 175 mm, i.e. about one-sixth free-space wavelength at 0.3 GHz. Mutual coupling between the radiating elements is significant in determining the array performance. The physics behind the TSA array is not well understood.

A dual-polarised wide-band and wide-angle scanning TSA array was reported in [CS00]. Its bandwidth is in the order of 5:1 over a scan volume of $\pm 45^\circ$. Based on [CS00], the key parameters that affect the overall array performance are the size of the slotline cavity, the length of the tapered slotline and the opening rate of the exponential taper. However, there are anomalies in the H-plane for the triplate structure. Vias along the slotline and the slotline cavity were introduced to eliminate impedance anomalies or resonance for both the dual-polarised tapered slot arrays [HCS00]. The single plate structure is used in this study to avoid the resonance in the operational band.

This type of antenna exhibit low cross-polarisation characteristics in the principle planes, however in the diagonal plane the co- to cross-polarisation ratio decreases rapidly away from boresight [LLK03]. It is indicated in [LLK03] that this high cross-pol components mainly stem from extensive surface currents flowing in the longitudinal direction along the element, and partly from unbalanced feed ports. Therefore, the radiation tapered slotline plate can be corrugated along the edges to reduce the surface currents along the longitude direction.

The Vivaldi antenna aperture with the exponential taper profile exhibits poor VSWR performance with a broad scan angles in the H-plane. It is the main limitation of the array

performance. A new curve is employed to form the taper profile and it shows a significant performance improvement when the array scans.

The parameter study for TSA arrays is presented in this chapter. The scan performance with an optimised TSA array with the new slotline profile is reported.

1.1.2 First Prototype

A triplate taper slot antenna is simulated and built. The element is shown in Figure 1.1. The measured and predicted return loss performance is shown in Figure 1.2. It is noted that the measured result is slightly better than the predictions in the low and high frequency end. The element aperture height is small compared with wavelength in the low frequency band, the cutoff frequency is about 600 MHz. Two large metal sheets were perpendicularly put at both end of the triplate. The aim is to improve the performance in the low frequency end. The return loss performance is shown in Figure 1.3. The same metal sheets are displaced from the triplate in the H-plane as shown in Figure 1.4. The distance from the metal sheet to the triplate is half the width of the triplate (i.e. 85mm). The return loss for the single element with displaced metal sheets in the H-plane is shown in Figure 1.5. It shows a significant return loss performance across the band. However, an optimised performance can be achieved by moving the metal sheets at both sides of the triplate. This is shown in Figure 1.6.

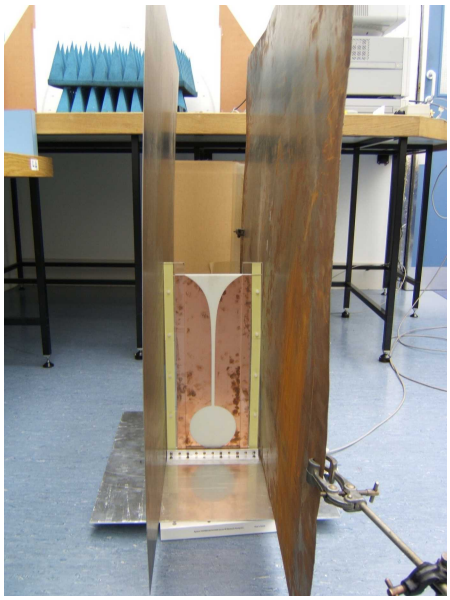

Figure 1.1: The first prototype of tapered slot antenna with triplate structure.

1.1.3 Second Prototype

Eight elements have been built to make a 2×2 dual-pol array. The infinite linear array formed by this element can cover the entire frequency band with reasonable impedance matching (VSWR ≤ 2). The elements built are shown in Figure 1.7. The return loss performance for the infinite linear array formed by this element is shown in Figure 1.8. The

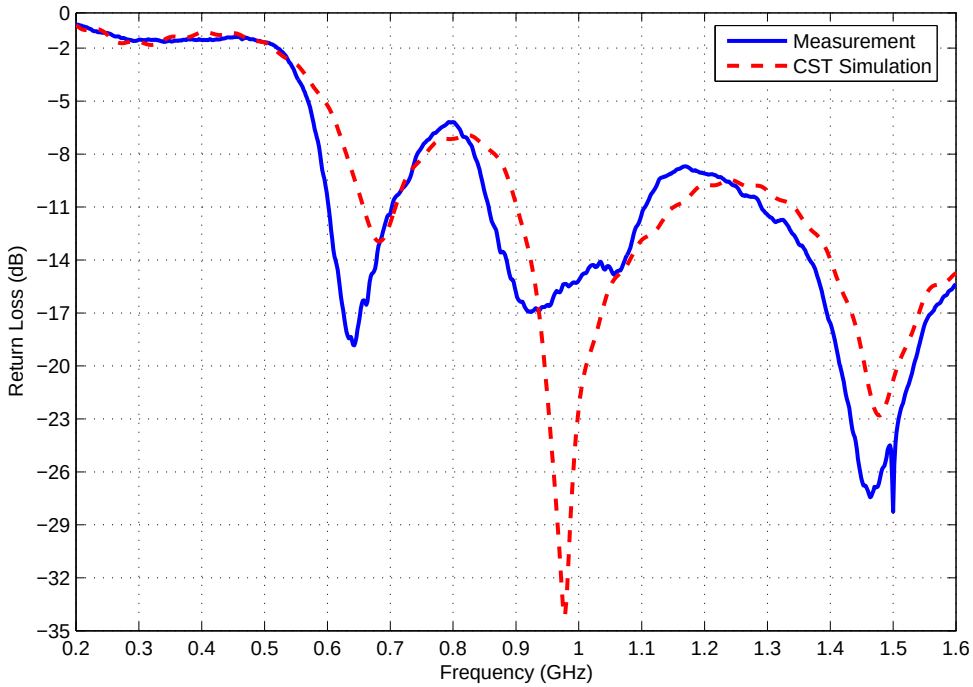

Figure 1.2: The return loss performance of the first prototype built.

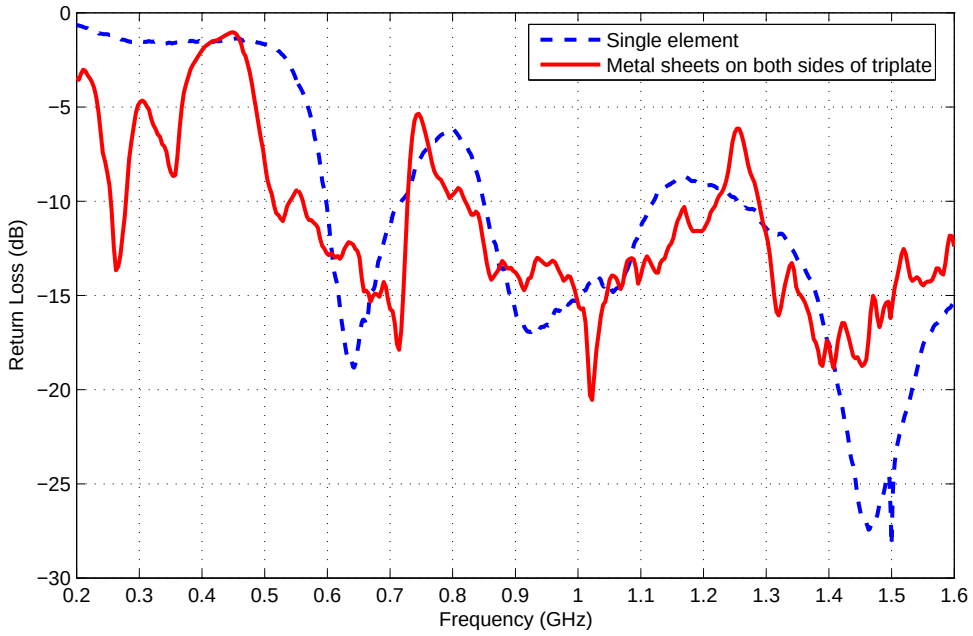

Figure 1.3: The element is grounded on both sides with large metal sheets.

Figure 1.4: The triplate tapered slot element is parallelled with two metal sheets in the H-plane.

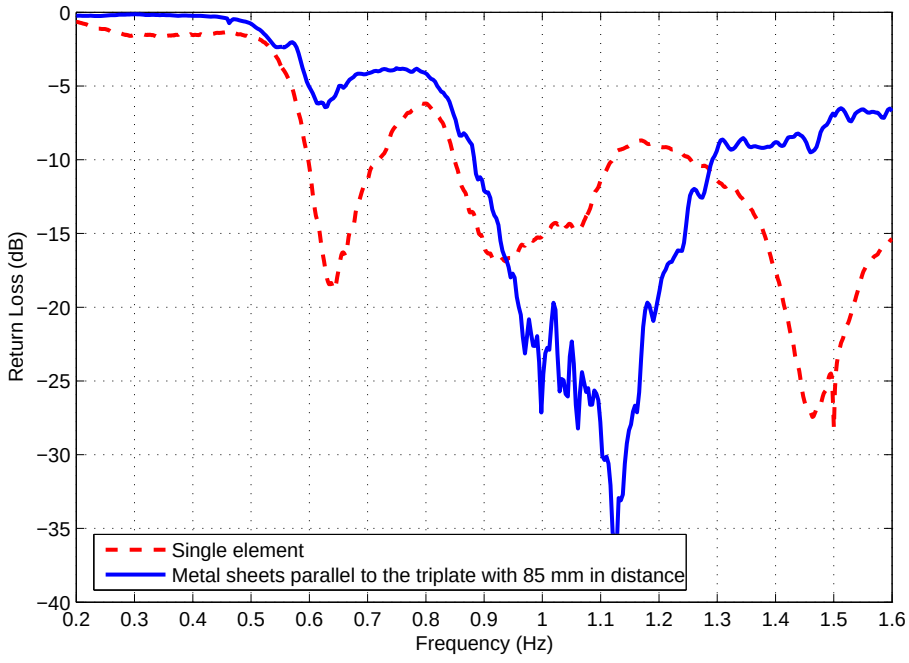

Figure 1.5: The element is parallelled with metal sheets in the H-plane with spacing to the metal sheet of 85 mm.

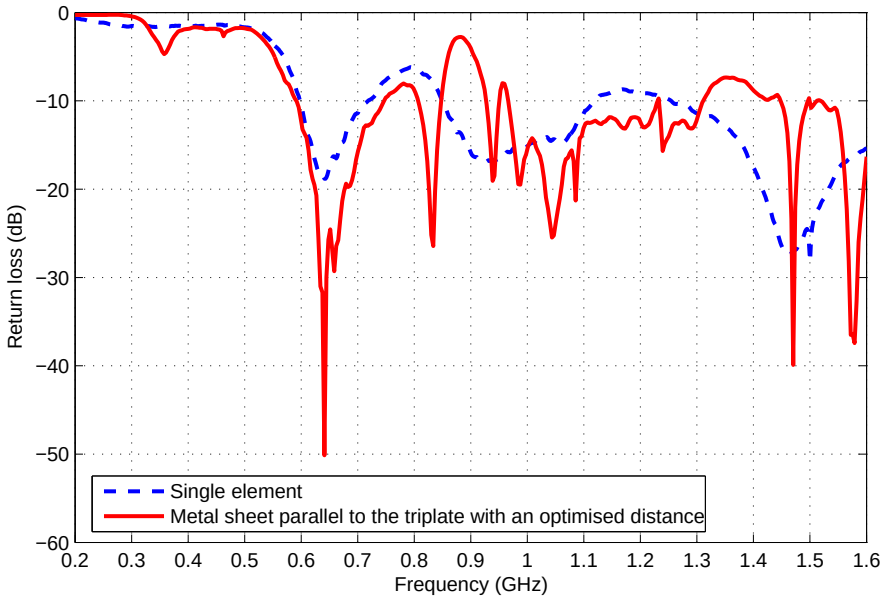

Figure 1.6: A better matching can be achieved by moving the metal sheet in the H-plane.

simulation and measured results are compared in Figure 1.9. The return loss for each element in the 4×1 linear array is shown in Figure 1.10. It is shown that elements in the middle of the linear array have better impedance matching. The coupling between the adjacent elements has significant effect on the performance in the low frequency end.

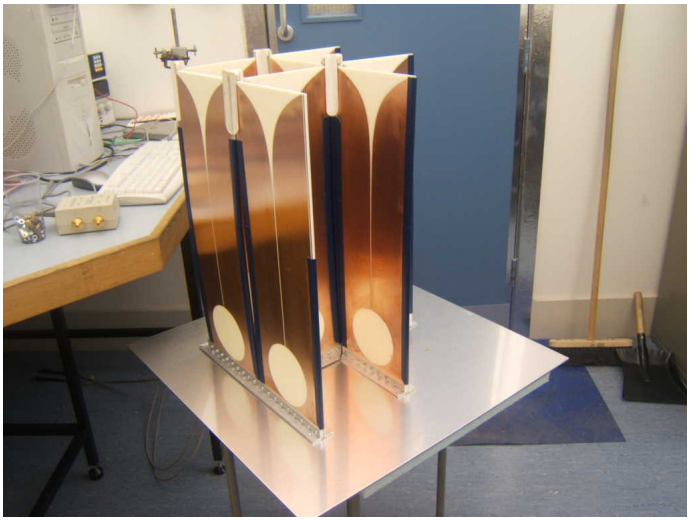

Figure 1.7: The second prototype with a triplate structure.

1.1.4 Vivaldi Antenna with the Exponential Taper Profile

The classic way to create the Vivaldi element is to couple the stripline feed to bilateral slotline in the ground planes. As shown in [CS00], the triplate structure shows several

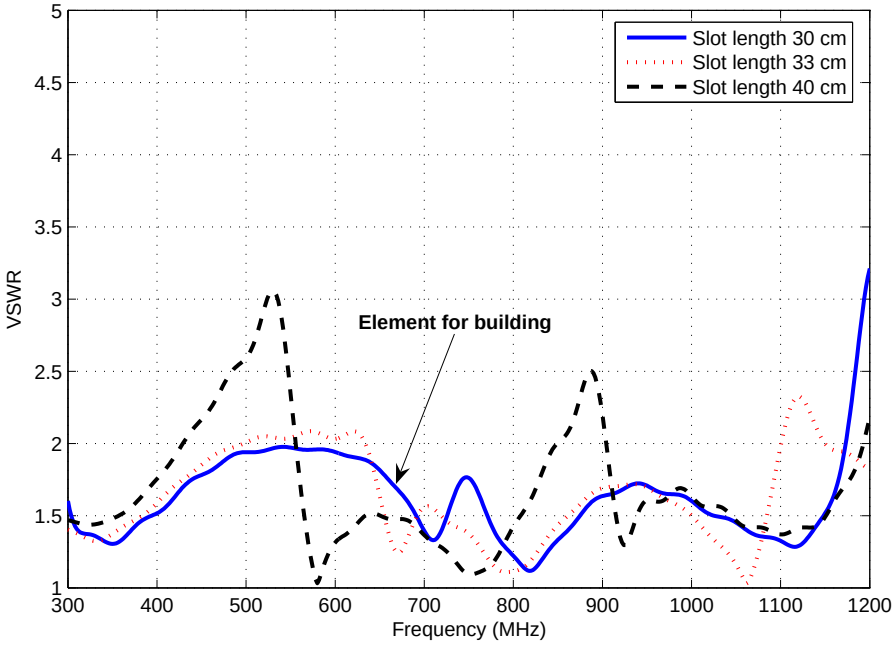

Figure 1.8: VSWR of the infinite linear array formed by the second prototype of triplate Vivaldi element.

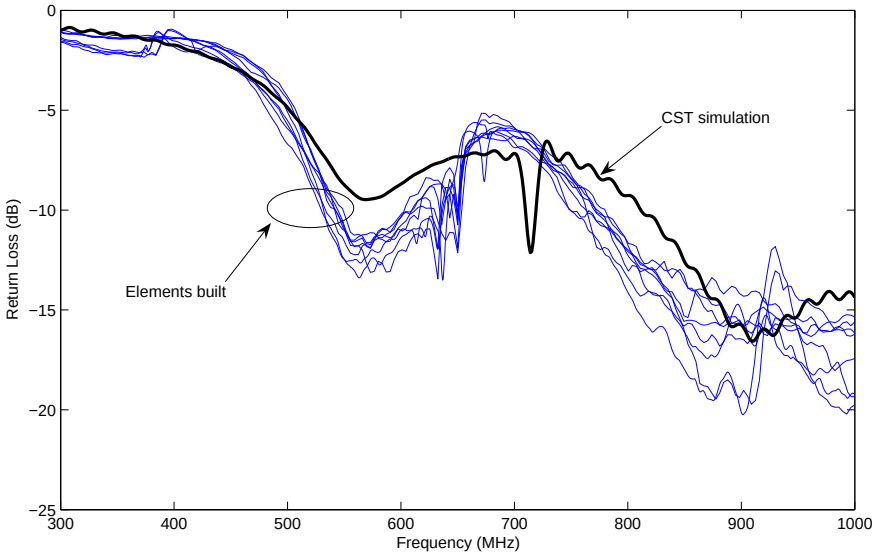

Figure 1.9: Return loss comparison between measurement and prediction for single elements.

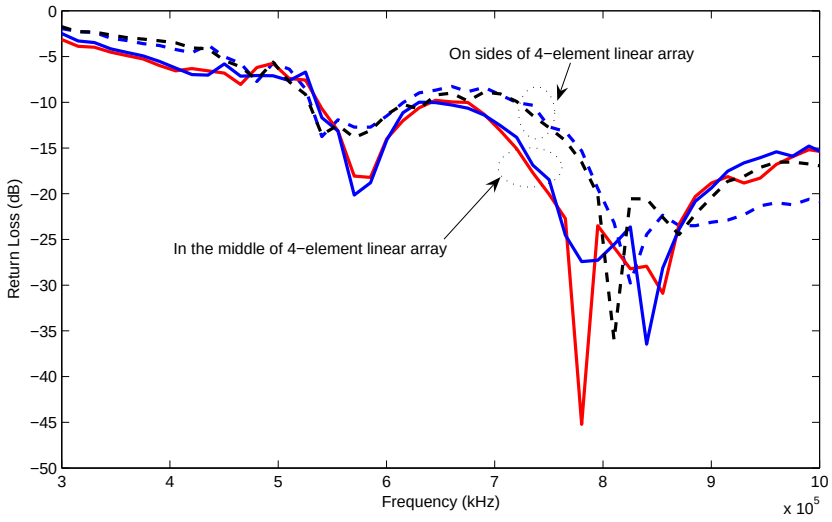

Figure 1.10: Return loss for the 4×1 linear array.

strong resonances through the entire usable frequency band. Therefore, a single plate structure is used to build the elements. This is shown in Figure 1.11.

(a) (b)

Figure 1.11: Tapered slot antenna element with a single metal plate, the slotline profile is defined by an exponential equation, (a) The stripline feed is terminated in a radial line stub, (b) The single-sided slotline is terminated at one end with a circular slot cavity.

Throughout the report, the following parameters are used to define the taper slot antenna element with a single metal plate:

It is difficult to achieve a good scan performance for the taper slot antenna elements with the exponential curve taper profile. A lobe at the middle of the operational band deteriorates VSWR performance when the array is scanned at 45° in the H-plane. Extensive simulations were conducted to achieve a wide scan angle. Figure 1.12 shows the VSWR performance when the array is being scanned at various angles in the H-plane. It is quite vivid that a big lobe appears at the middle of the operational band for large scan angles.

R_r	Radius of radial stripline stub
C_r	Radius of the circular slotline cavity
L_s	The taper length
H	The aperture height
w	The E-plane spacing
L	Offset of slotline cavity from the ground plane
dsl	Slotline width
fsl	Stripline width

Table 1.1: Taper Slot Antenna Element Parameters

1.1.5 Vivaldi Antenna with the New Taper Profile

A new taper profile proposed by BAE is employed to construct the taper slot profile. The single plate structure is shown in Figure 1.13. The curve to build the taper slotline is given as the following:

$$x = (1 - e^{-\alpha z})^p \tag{1.1}$$

where x is the transverse distance starting from the slot line edge, z is the longitudinal distance along the slot line. Here $\alpha = 1$, $p = 3$ is used to build the profile in the single metal plate vivalid design. The element with a slot aperture built from this profile can achieve much better VSWR performance than the element using an exponential curve profile, especially in the middle of the operation band for SKA.

First, the following parameters are used to build the element: $R_r = 24$ mm, $C_r = 15$ mm, $H = 140$ mm, $L_s = 280$ mm, $L = 15$ mm, $w = 170$ mm, $dsl = 1.2$ mm, $fsl = 1.8$ mm.

Since the H-plane has the worst performance and the E-plane has the best. VSWR performance for the large scan angles (40° and 45°) in the H-plane is shown in Figure 1.14 We note the array with 170 mm element spacing can achieve 40° scan with a reasonable VSWR performance.

For boresight scan, the low frequency performance is limited by a rapid decrease in the input impedance. Larger slotline cavity can increase the input impedance at the low frequency and accordingly improve the VSWR. However, when the array is scanned to 45° in H-plane, the VSWR goes worse as the slotline cavity increases. This is shown in Figure 1.15.

The element (aperture height $H = 140$ mm, element separation spacing $w = 170$ mm), shows higher VSWR (VSWR ≥ 2, but less than 3) from 300-500 MHz when the array is scanned to 45° in the H-plane. The height of the tapered slot aperture and the length of the slotline have been adapted to improve scan performance in the low frequency band. By changing the length of the taper slot and the height of the aperture, the boresight scan performance has a significant improvement. The structure with larger circular slotline cavities has worse 45° scan performance at H-plane than the structures with smaller slotline cavity sizes. This is shown in Figure 1.16.

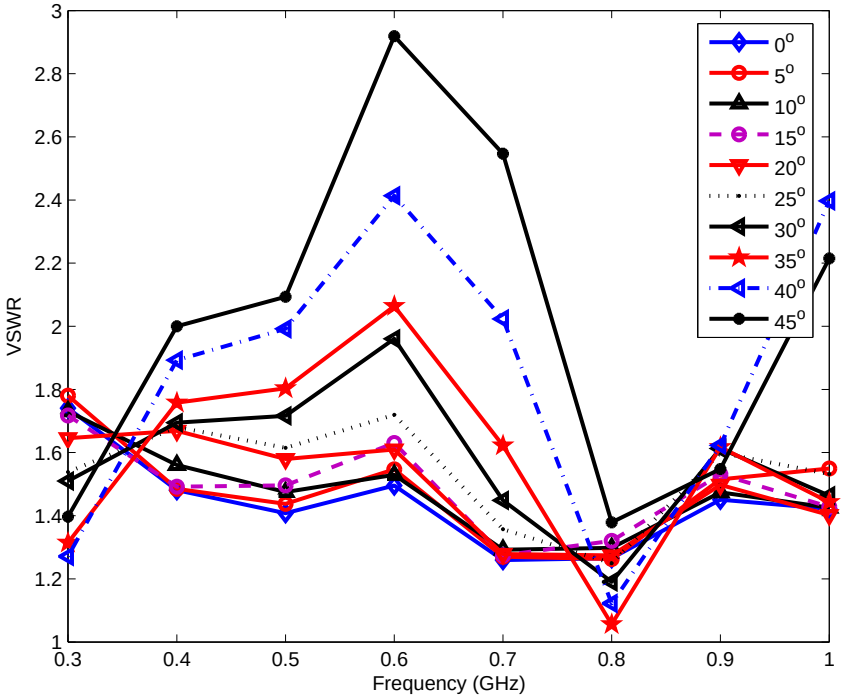

Figure 1.12: Tapered slot antenna array is being scanned in the H-plane.

(a) (b)

Figure 1.13: Tapered slot antenna element with a single metal plate, the slotline profile is defined by the new curve equation (a) The stripline feed is terminated in a radial line stub, (b) The single-sided slotline is terminated at one end with a circular slot cavity.

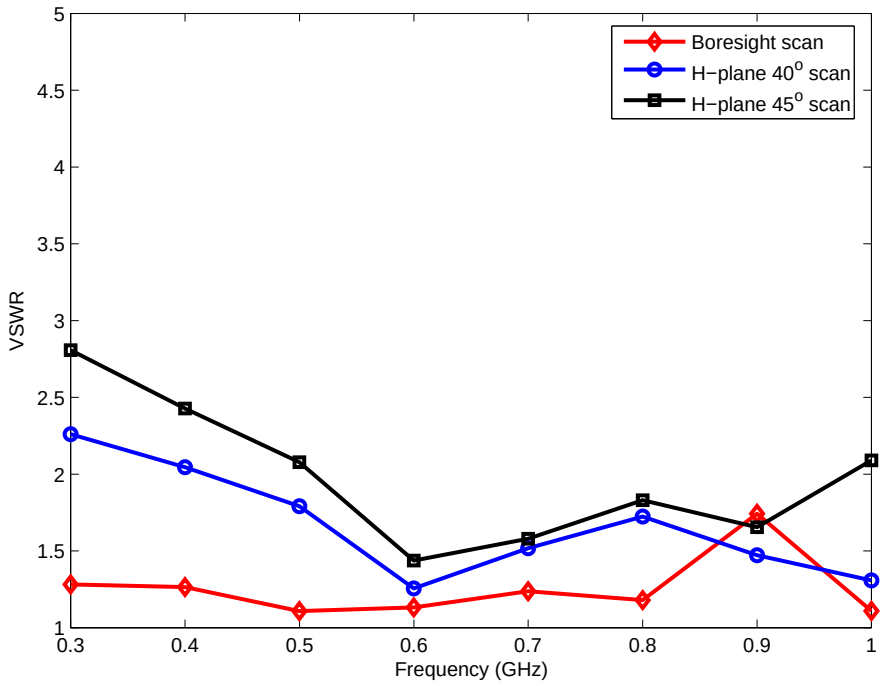

Figure 1.14: The boresight and large scan angles in the H-plane, the element spacing of $w = 170$ mm.

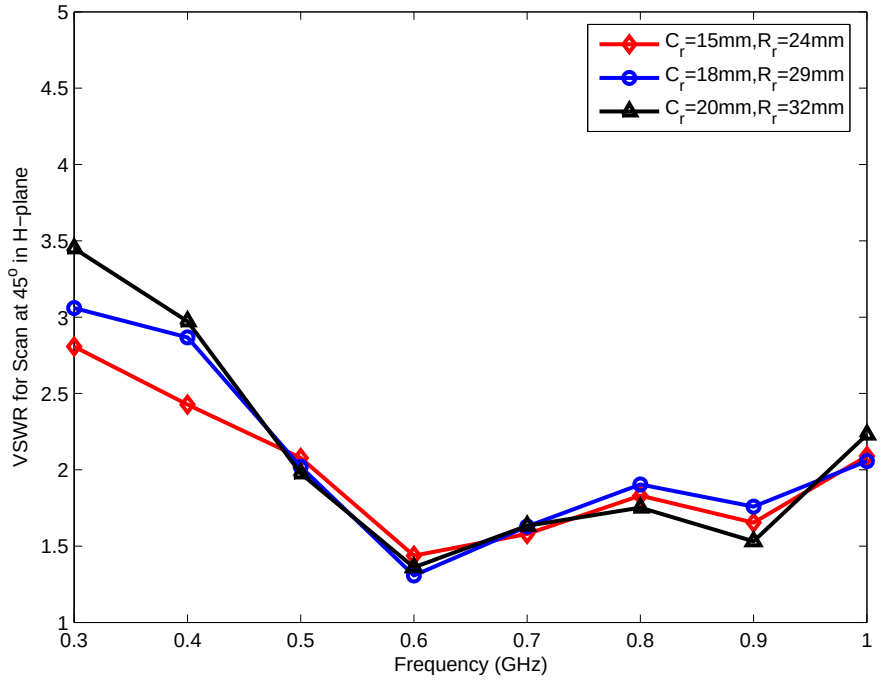

Figure 1.15: The scan performance at 45° in the H-plane changes with the size of slotline cavity.

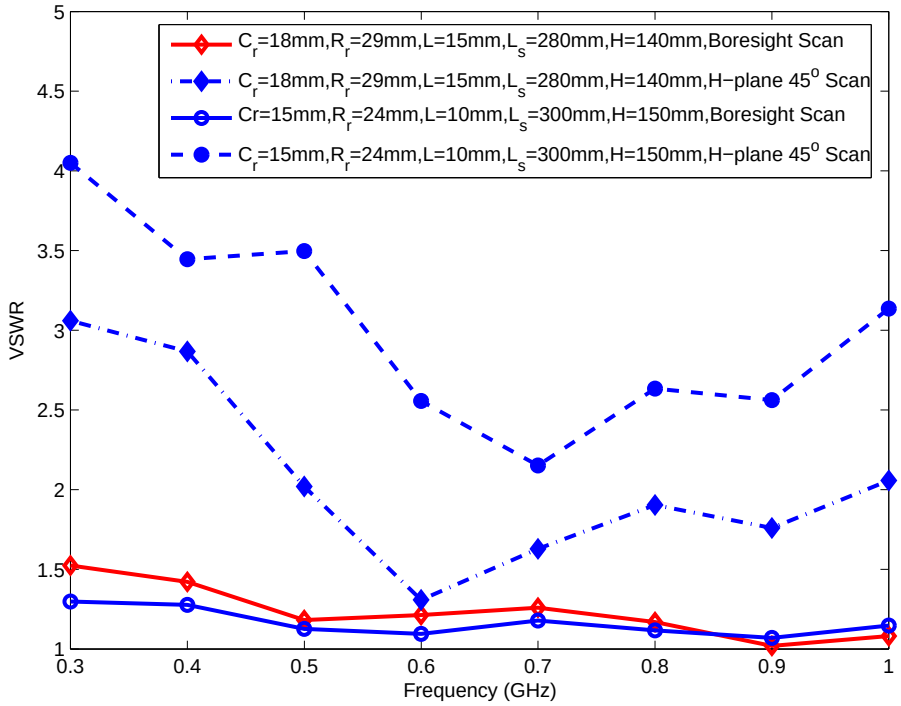

Figure 1.16: Scan performance for the elements with different slotline lengths and apertures.

1.1.6 Solver Cross Check

Cross check has been conducted to verify the array performance by extending the "Unit Cell" to infinity in both CST and HFSS. The CST MWS can work in both frequency and time domains. However, the Transient Solver based on the time domain solution can't introduce phase shift among the unit cell boundaries, the boresight scan performance can be approximately predicted by the time domain solver. The structure shown in Figure 1.17 is used as a "Unit Cell" model to compare the array performance in both CST and HFSS. The boresight scan performance is shown in Figure 1.18. The frequency domain solvers show significantly different results. Therefore the cross check process is essential to predict element performance in an infinite array.

1.2 Comb-Line Taper Slot Antenna

1.2.1 Comb-Line TSA

Tapered slots have been widely used for different applications. However the continuous metal plate structure can potentially introduce higher order modes along the E-plane. Therefore, high cross-pol components are produced in the principle planes; it is even worse in the diagonal cut (45°). One of the reasons is from the extensive surface current along the continuous plate.

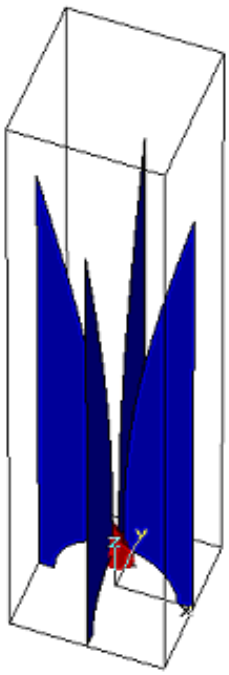

Figure 1.17: The unit cell of the Vivaldi element in the CST MWS for cross check.

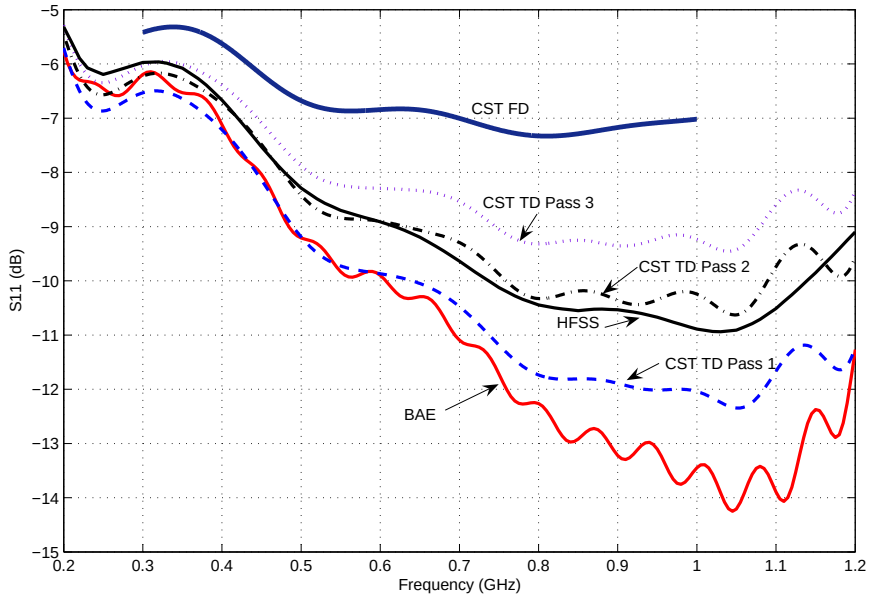

Figure 1.18: Return loss of an infinite array being scanned to the boresight, the results are compared from different solvers.

Corrugation on the E-plane is used to suppress the surface current along the longitudinal direction. The structure is shown in Figure 1.19, the chocks are corrugated along the edge of the metal plate.

It has shown two benefits from the corrugation; the comb-line design improves the return loss performance at the low and high frequency ends for the H-plane scans. This is shown in Figure 1.20. Another improvement is to make the elliptical polarisation in the D-plane less dependent on frequency. This has significant benefit for polarisation calibration across the band. The VSWR performance for H-plane scans is compared in Figure 1.20 for the antenna element with and without corrugation. The axial ratio for scan at 45° in the D-plane is shown in Figure 1.22.

(a) (b)

Figure 1.19: Combline tapered slot antenna with a new slotline profile, (a) Comb-line tapered slot antenna fed by a strip line terminated in a radial line stub, (b) Comb-line tapered slot antenna with a new profile curve.

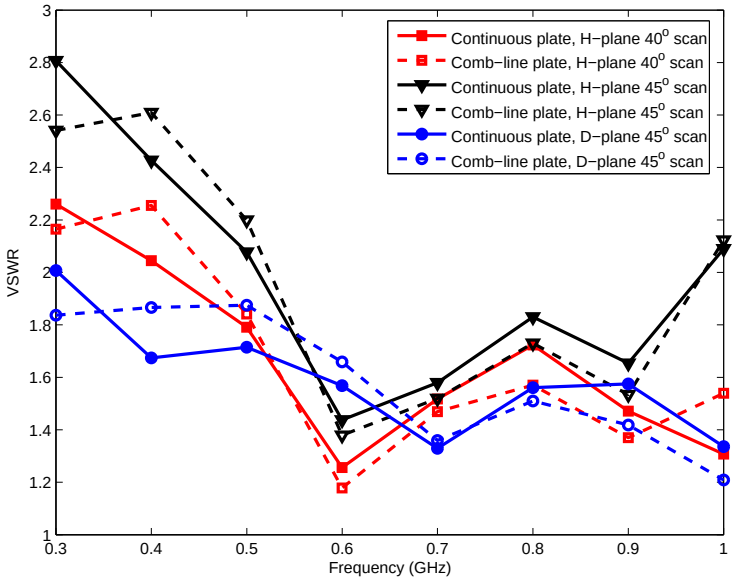

Figure 1.20: The scan performance in the H-plane of the tapered slot element with a continuous plate or a comb-line plate.

It should be pointed out that the comb-line plate with $w = 170$ mm shows performance drop at the frequency range of 300 MHz to 500 MHz when the array is being scanned

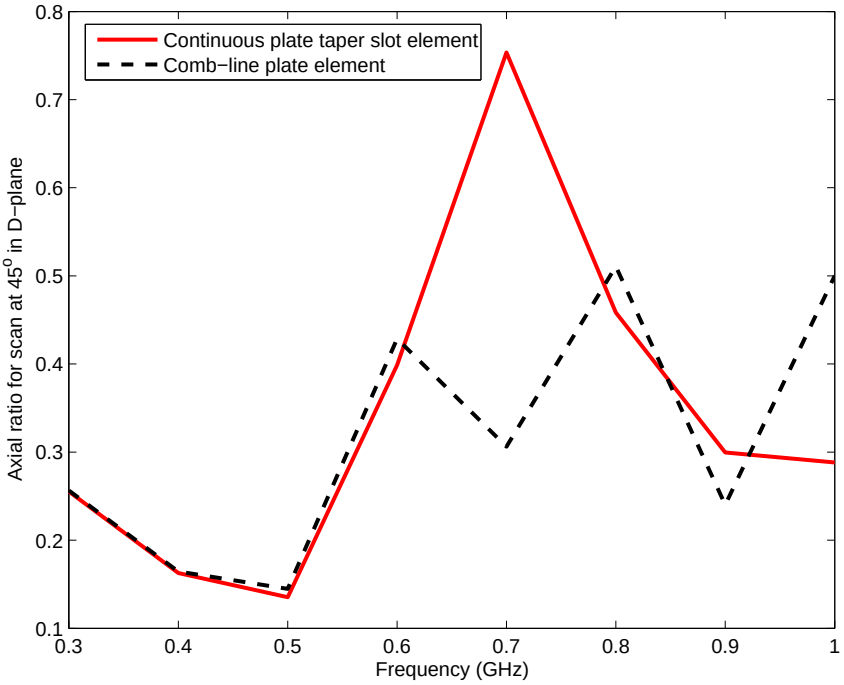

Figure 1.21: The axial ratio for the array being scanned to 45° in the D-plane, the tapered slot element with a continuous plate or a comb-line plate.

to 45° in the H-plane. Therefore, both a wider plate with $w = 175$ mm and a smaller structure with $w = 160$ mm are employed. The VSWR performance for scan at 45° in the H-plane is shown in Figure 1.22. The wider plate with $w = 175$ mm and the length of slot line $L_s = 300$ mm shows overall better performance than any other scenarios with a plate of narrower width.

A metal pole is introduced between the elements to reduce the coupling between them, the 45° scan performance is shown in Figure 1.23, there is no significant effect due to this metal pole. The VSWR performance for the array with the element width $w = 175$ mm and $L_s = 300$ mm is shown in Figure 1.24 when the array is scanned in the H-plane.

When the width of plate increase, the VSWR performance at low frequency improves. The separation spacing between the elements are increased, therefore, the grating lobes are expected to appear. For the element with separation distance of 175 mm, the 10×10 elements pattern for scan at 45° in H-plane is given in Figure 1.25. A grating lobe appears at the opposite direction. However, it is out of the scan range.

In order to improved the scan performance in the low frequency end, the length of the tapered slotline (L_s) is extended to 35 cm while the height of the aperture (H) is kept the same. The scan performance at the low frequency end has been improved. The VSWR values are less than 2 across the frequency band in the scan volume except that a small lobe appears at 400 MHz when the array is scanned to 45°. This is shown in Figure 1.26.

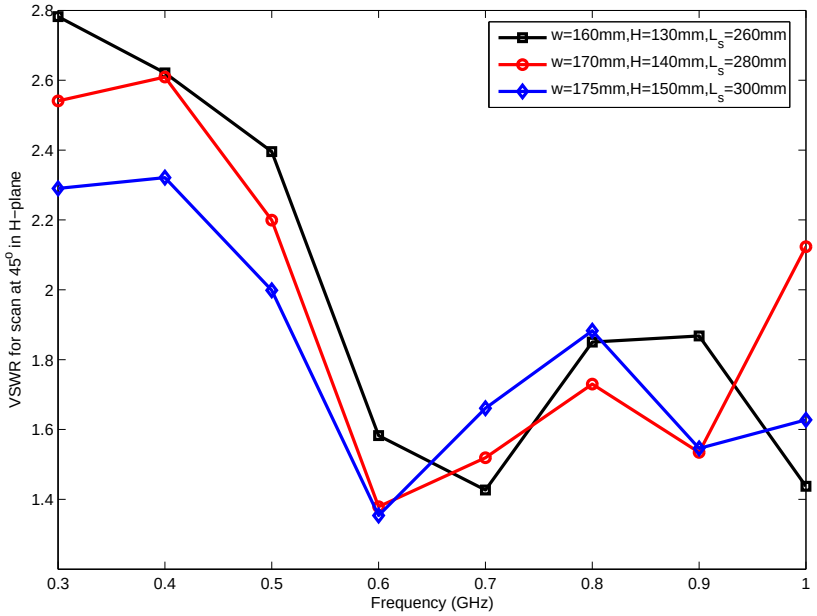

Figure 1.22: VSWR performance of the comb-line element being scanned to 45° in the H-plane, the element has different slotline lengths, aperture height and element separation spacing.

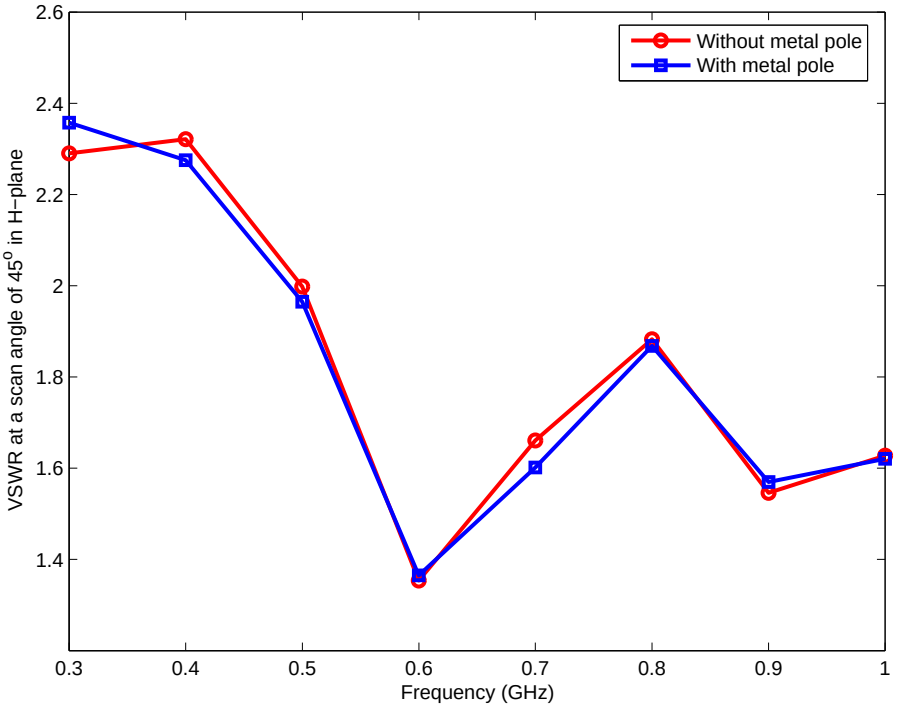

Figure 1.23: The performance for 45° scan in the H-plane with and without the metal pole between elements, the comb-line element of $w = 175$ mm, $H = 150$ mm.

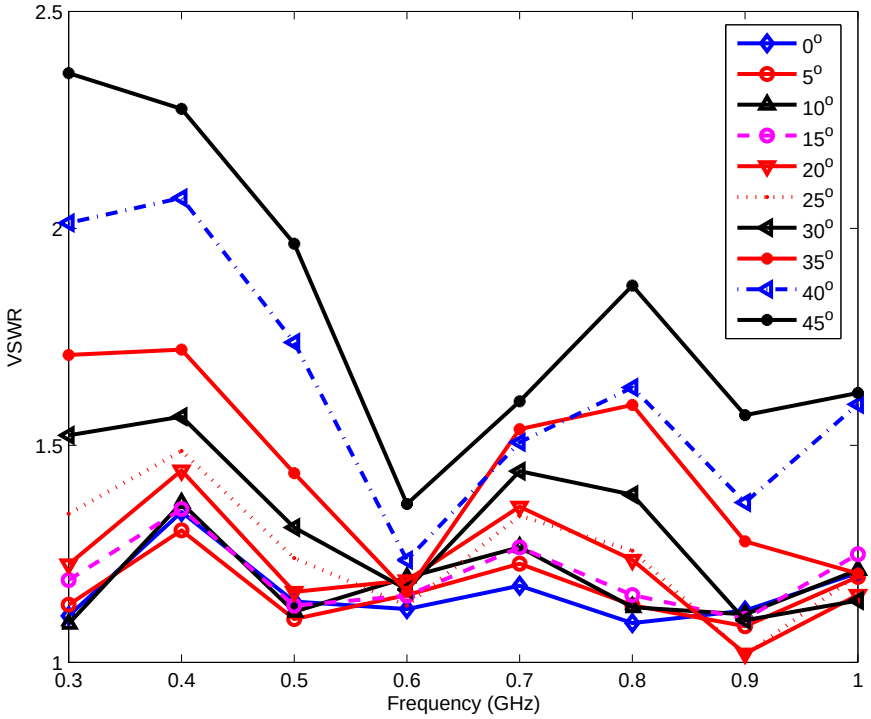

Figure 1.24: The VSWR performance when the array is being scanned in the H-plane, the comb-line element has $w = 175$ mm, $H = 150$ mm, $L_s = 300$ mm.

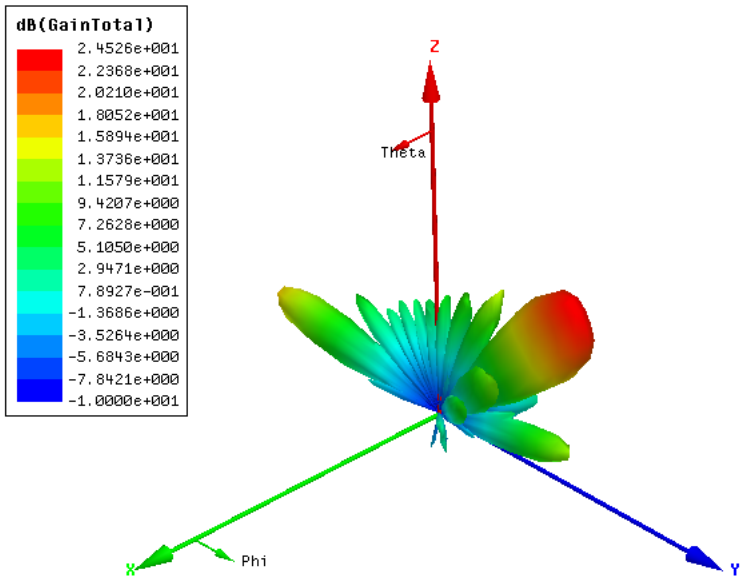

Figure 1.25: 10×10 comb-line taper slot antenna array being scanned to 45° in H-plane, the element separation spacing $w = 175$ mm, the slot aperture height $H = 150$ mm.

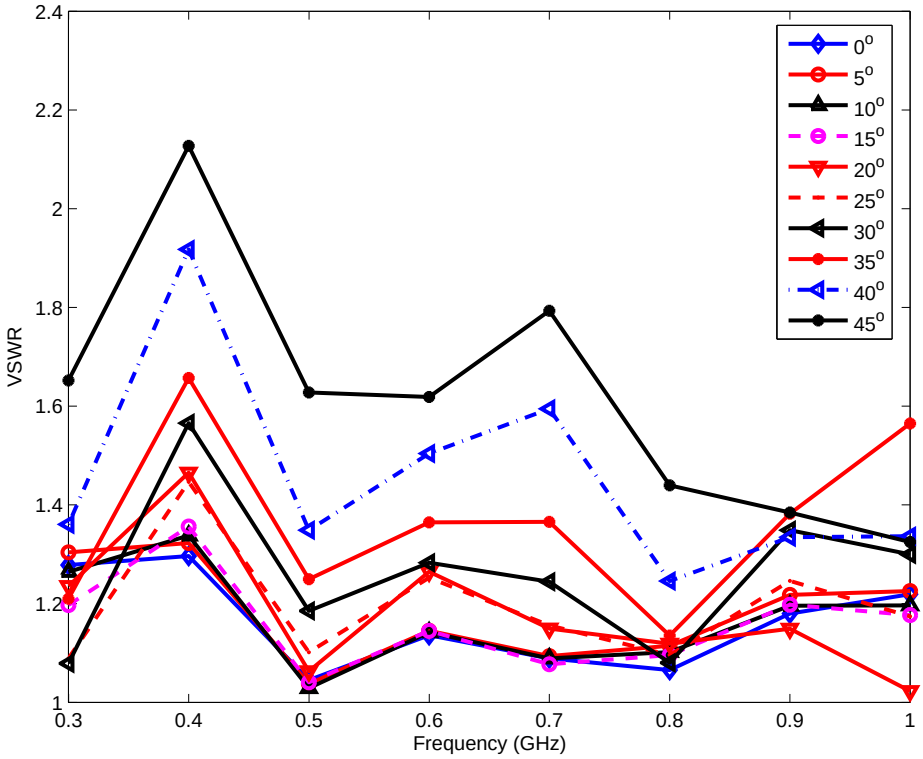

Figure 1.26: The VSWR performance when the array is being scanned in the H-plane, the comb-line element has $w = 175$ mm, $H = 150$ mm, $L_s = 350$ mm.

1.3 Bunny Ear Antenna

The high cross-pol performance for the Vivaldi antennas may come from two sources: the excessive current flows along the longitude direction; the other source may stem from the unbalanced feeding scheme. Bunny ear type of antenna can achieve better cross-pol performance by cutting the lower part of the plate close to the ground plane, hence the current along the metal plate can be suppressed. The element is shown in Figure 1.27. It is noted that the axial ratio in the diagonal plane is much smaller than the Vivaldi design and shows close-to-linear polarisation in both principle and diagonal planes. On the other hand, the plate is much shorter than the Vivaldi element. However, this design works best with a balanced feeding scheme, although it was reported that a coaxial cable was successfully used for feeding directly. The cable feeding scheme needs an impedance transformer changing the characteristic impedance of the slot (i.e. 120 ohms in the case) to the impedance of the cable (i.e. 50 ohms).

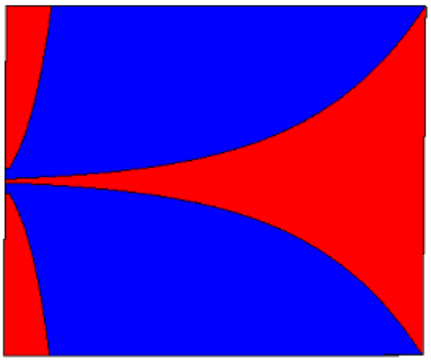

Figure 1.27: The double layers of copper bunny ear element, the element spacing in the E-plane of 170 mm.

The scan performance for the bunny ear antenna array is shown in Figure 1.28. The axial ratio for the scan at 45° in the D-plane is shown in Figure 1.29. A linear polarisation can be observed. An array with 10×10 bunny ear elements has been scanned to the boresight and 45° in the H-plane. The array patterns are shown in Figure 1.30 and Figure 1.31, respectively.

1.4 Munk Antenna

Munk antennas use a fundamentally different approach to design the wideband array [Mun03]. Mutual coupling is intentionally introduced between the array elements. Initially work start with coupled dipoles. The capacitance between the ends of dipoles is introduced to

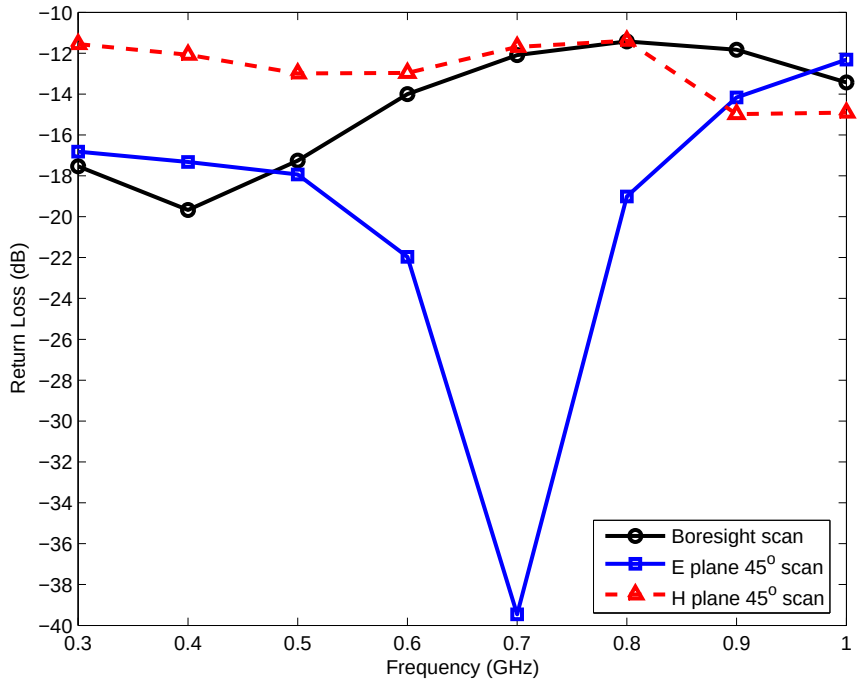

Figure 1.28: Return loss of the bunny ear antenna for different scan angles.

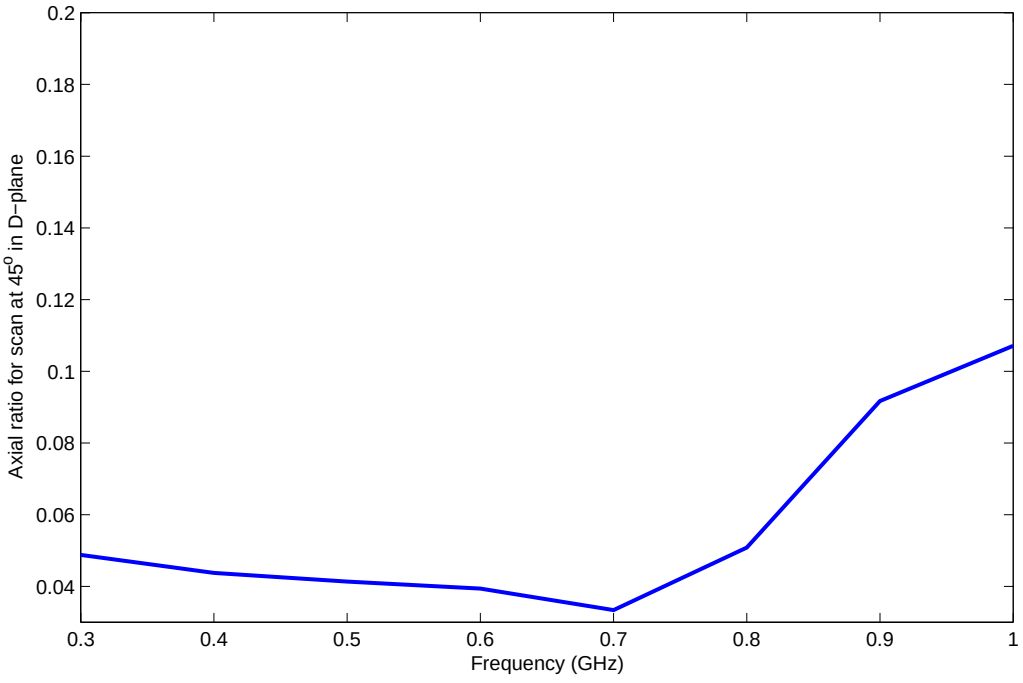

Figure 1.29: Axial ratio for 45° scan in the D-plane with the bunny ear array.

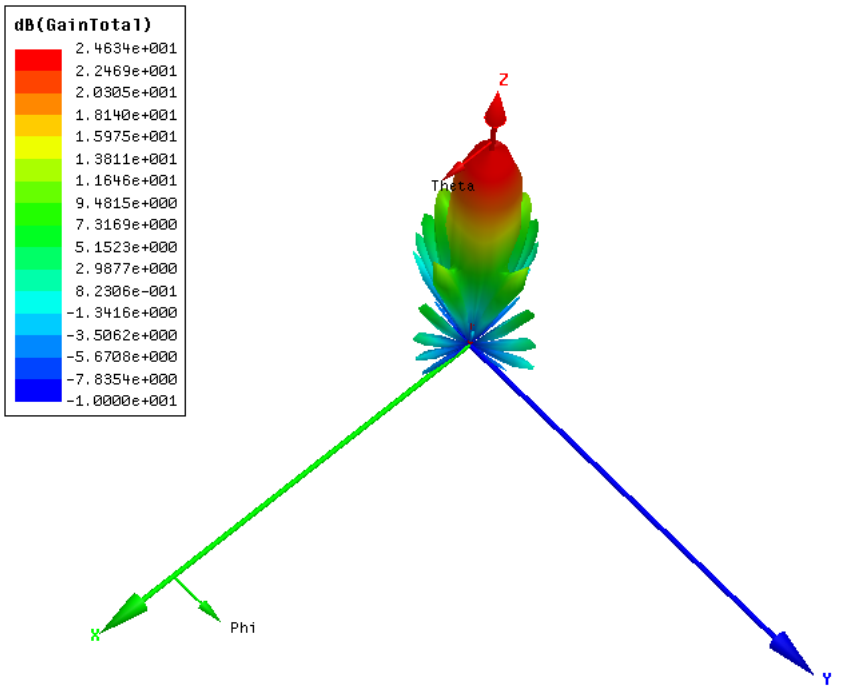

Figure 1.30: The array boresight scan pattern for 10×10 bunny ear elements array.

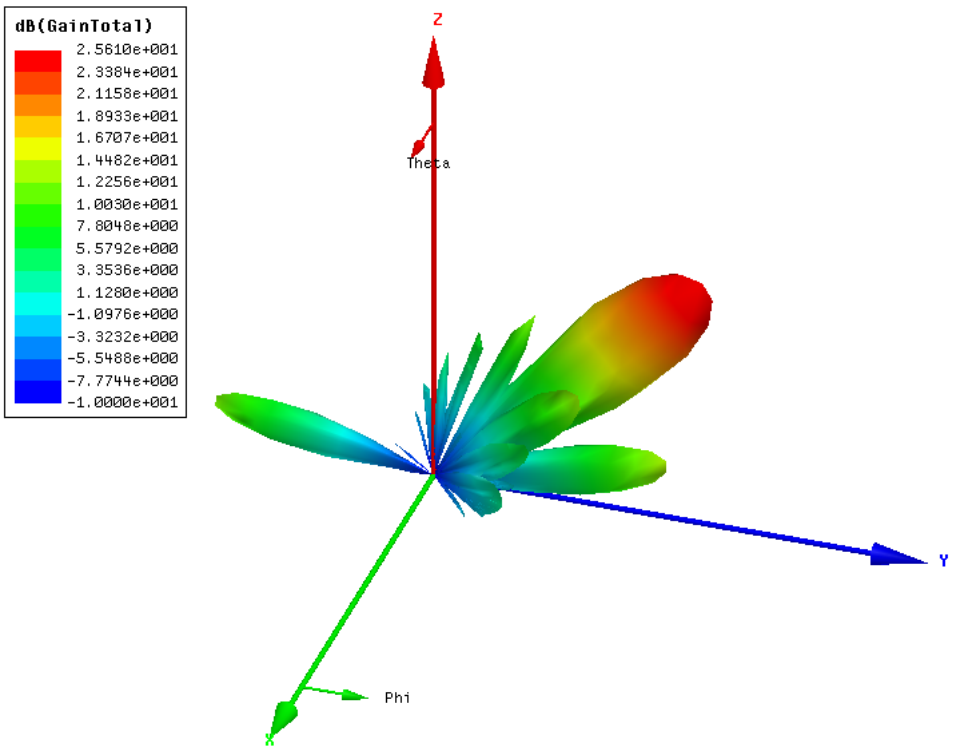

Figure 1.31: H-plane 45° scan pattern for 10×10 bunny ear elements array, the element spacing of 170 mm.

make the bandwidth broader. An even broader bandwidth can be achieved by placing dielectric layers over the array. In complementary theory, slot elements are introduced to take advantage of their desirable broader element radiation patterns (compared to the dipole antennas). Inductors instead of capacitors are used to connect the ends of slots to yield field continuity.

1.4.1 Dipole Array Backed by a Groundplane

A single dipole antenna with the length of 170 mm (the maximum element separation distance for scanning at 45° at 1 GHz without grating lobes) distance shows a very narrow bandwidth. The Smith chart and the return loss performance for this single element is shown in Figure 1.32 and Figure 1.33 respectively.

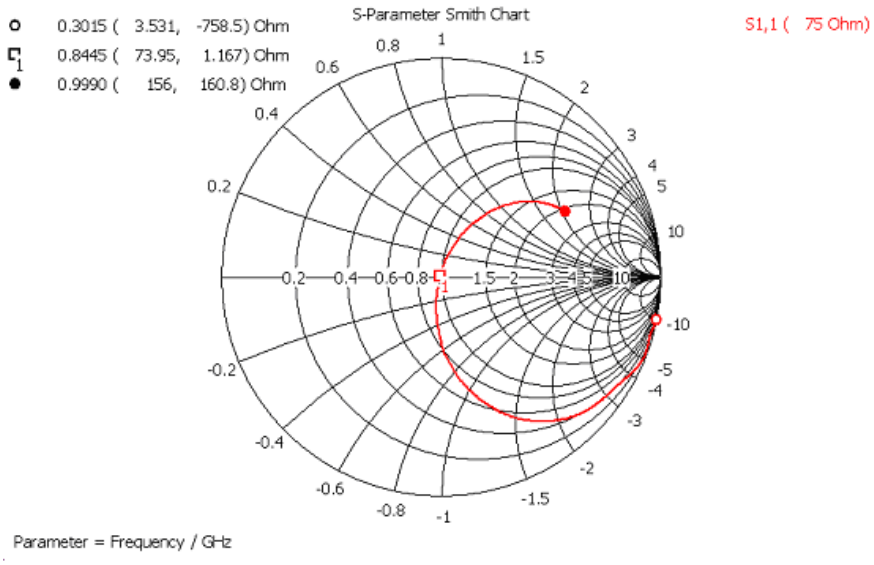

Figure 1.32: Smith chart for a single dipole antenna of length 170 mm. The arms of the dipole are metal sheets with width of 2 mm.

The 2-D infinite array for this element make the bandwidth broader than the single element. The input characteristic impedance changes from 75 ohms for the single element to 90 ohms for the infinite array. The Smith chart and the return loss for the 2-D infinite dipole array are shown in Figure 1.34 and Figure 1.35.

A groundplane is introduced aiming at broaden the operation bandwidth. The optimum distance between the array and the groundplane is searched by parametric sweeps in the simulations. This is shown in Figure 1.36. It is noted that the input impedance increase significantly with a back up groundplane. For fixed impedance of 90 ohms, the centre frequency for the array moves from 850 MHz to 760 MHz with the ground plane introduced. There is no significant gain in terms of bandwidth for small distances. It seems that the bandwidth becomes wider as the distance increases. For distance at 50 mm and 90 mm, the Smith chart and the return loss performance are shown in Figure 1.37 to Figure 1.40. The bandwidth for VSWR ≤ 2 is close to 400 MHz when the distance between the array and the groundplane is 90 mm. A finer parametric sweep is then conducted with the gap

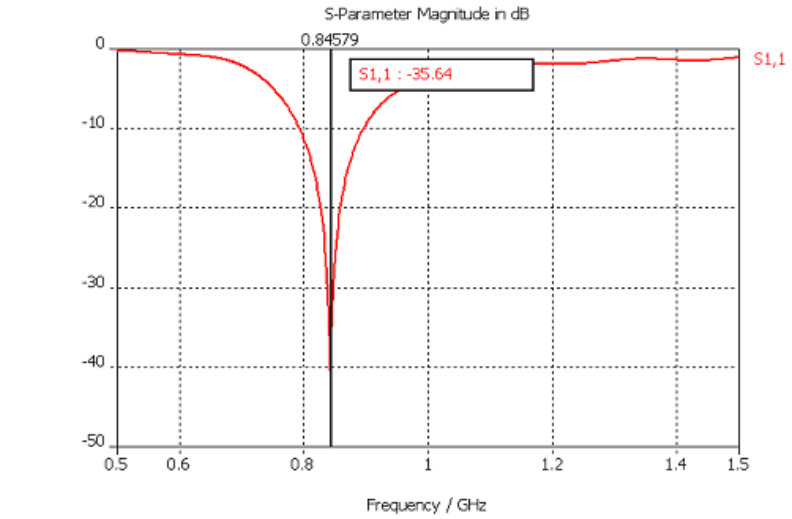

Figure 1.33: Return loss for a single dipole antenna with the total length of 170 mm.

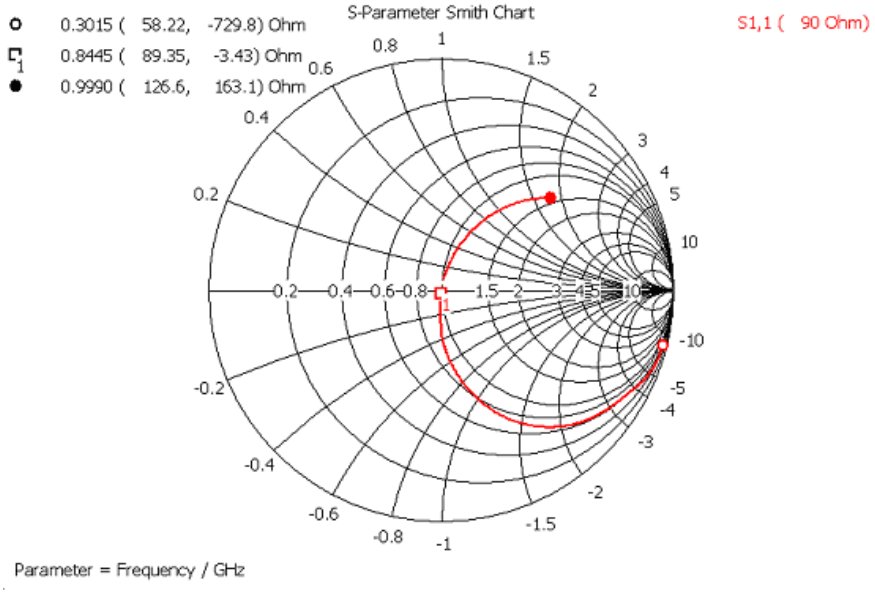

Figure 1.34: Smith chart for the infinite dipole array of element separation spacing 170 mm. The arms of the dipole are metal sheets with width of 2 mm.

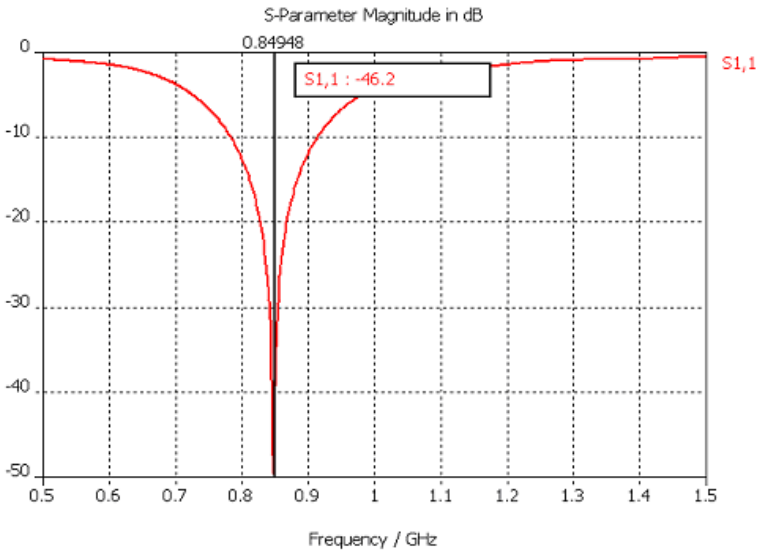

Figure 1.35: The return loss for the infinite dipole array, the separation spacing between element is 170 mm.

between the array and ground plane close to 90 mm. This is shown in Figure 1.41. The centre frequency as well as the operational bandwidth increases as the distance become larger. The input impedance becomes bigger as the distance increases.

In order to match the low frequency, 85 mm distance between the array and the ground plane is chosen to form the infinite array. The return loss as well as the Smith chart is shown in Figure 1.42 and Figure 1.43. For VSWR $\leq$ 2, 400 MHz bandwidth can be achieved.

It is reported in [Mun03] that a capacitor can be introduced between the ends of adjacent dipole elements to increase the mutual coupling between elements. Potentially the bandwidth may increase accordingly.

A capacitor with $C = 0.12732$ pF is connected between the dipole elements. The return loss and Smith chart is shown in Figure 1.44 and Figure 1.45, it is observed that the central frequency of the operation band moves down from 0.86 GHz to 0.65 GHz, the best match impedance increases from 175 ohms to 185 ohms. The bandwidth for VSWR ≤ 2 is about 300 MHz (i.e. from 550 MHz to 850 MHz).

The capacitor is then doubled from $C = 0.12732$ pF to $C = 0.12732$ pF $\times$ 2. The overall frequency bandwidth becomes narrower. The operational frequency band shifts towards lower frequencies. This infers that greater capacitance between elements doesn't always imply wider bandwidth. However it is beneficial to make the dipole array work in the lower frequency band. These are shown in Figure 1.46 and Figure 1.47.

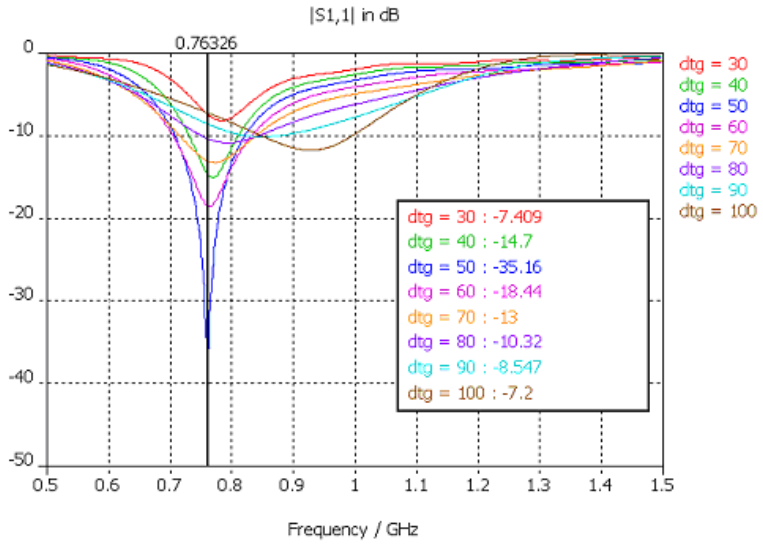

Figure 1.36: The return loss for the dipole array backed by a ground plane with various distances between them.

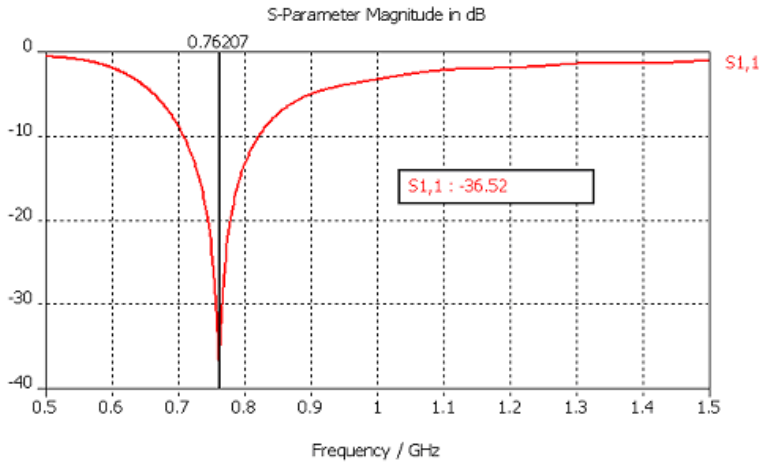

Figure 1.37: The return loss for the dipole array backed by a groundplane with 50 mm distance.

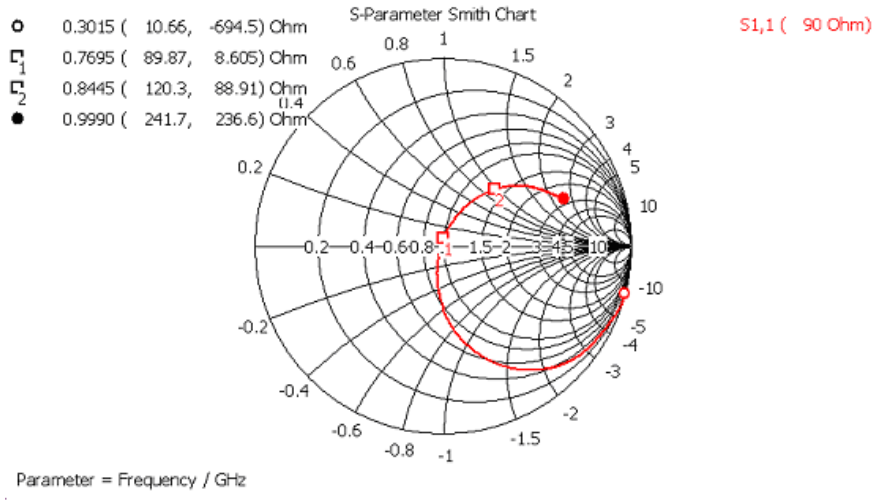

Figure 1.38: Smith chart for the dipole array backed by a groundplane and the distance between them is 50 mm.

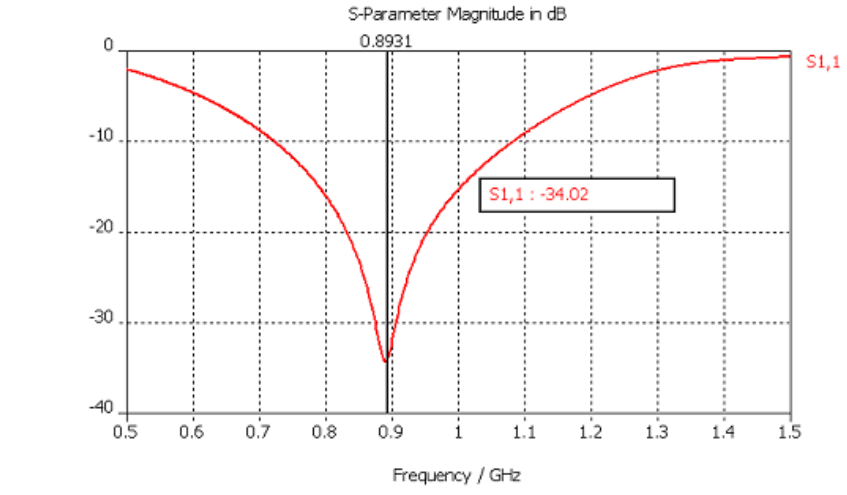

Figure 1.39: Return loss for the dipole array backed by a ground plane and the distance between them is 90 mm.

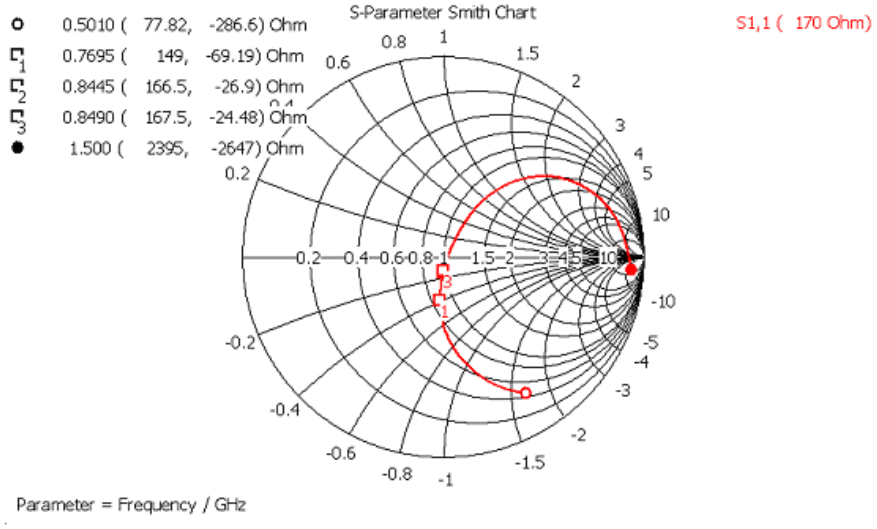

Figure 1.40: Smith chart for the dipole array backed by a ground plane and the distance between them is 90 mm.

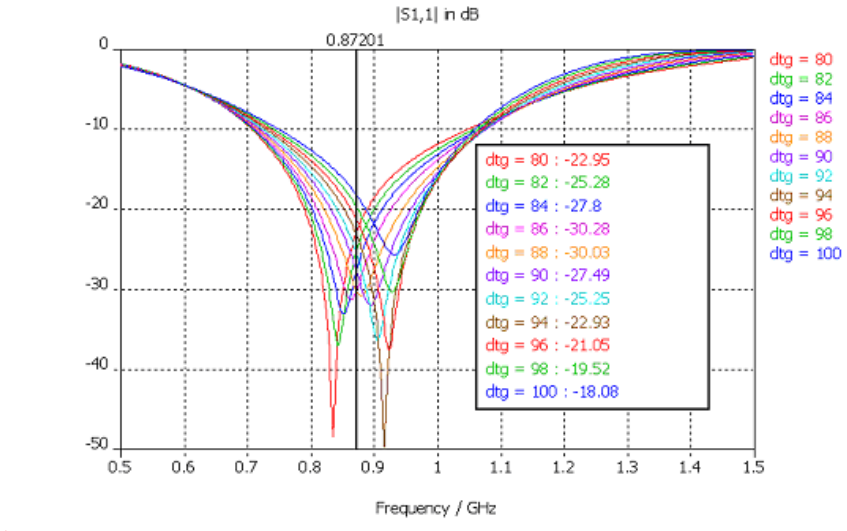

Figure 1.41: Return loss changes with the distance between the dipole array and the ground plane. The impedance is normalised to 175 ohms.

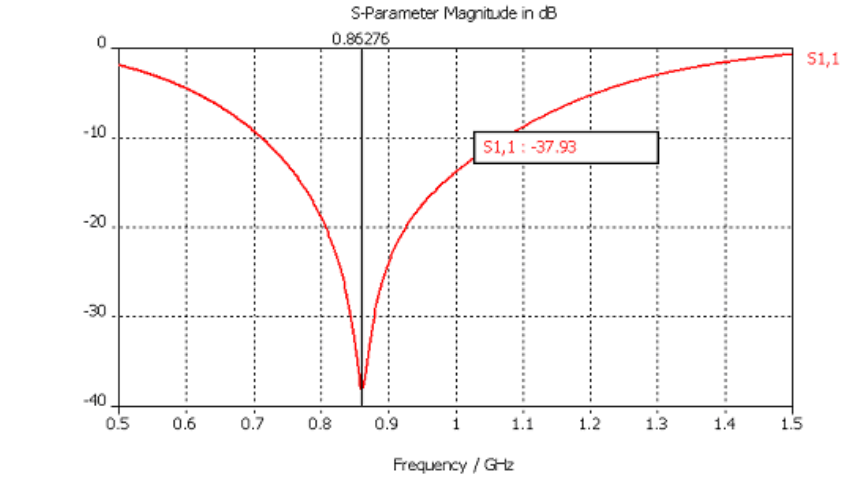

Figure 1.42: The return loss for the dipole array backed by a ground plane and the distance between them is 85 mm. The impedance is normalised to 175 ohms.

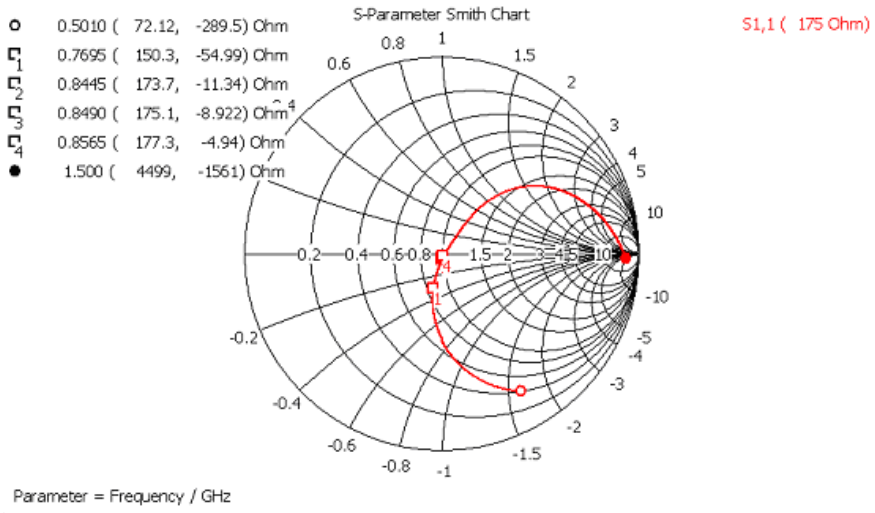

Figure 1.43: Smith chart for the dipole array backed by a groundplane and the distance between them is 85 mm.

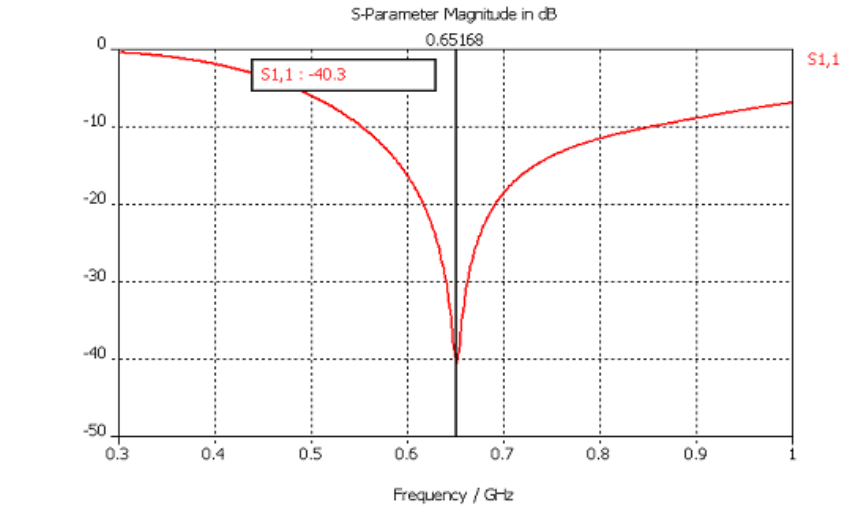

Figure 1.44: The return loss for the array backed by a ground plane and the distance to the groundplane is 85 mm, a capacitor with $C = 0.12732$ pF is used to connect the ends of adjacent dipole elements.

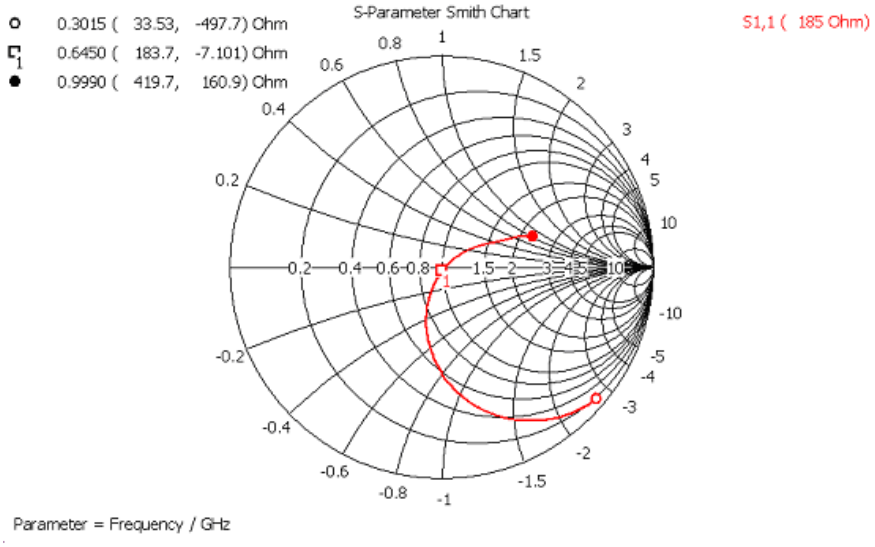

Figure 1.45: The Smith chart for the array backed by a ground plane and the distance to the ground plane is 85 mm, a capacitor with $C = 0.12732$ pF is used to connect the ends of adjacent dipole elements.

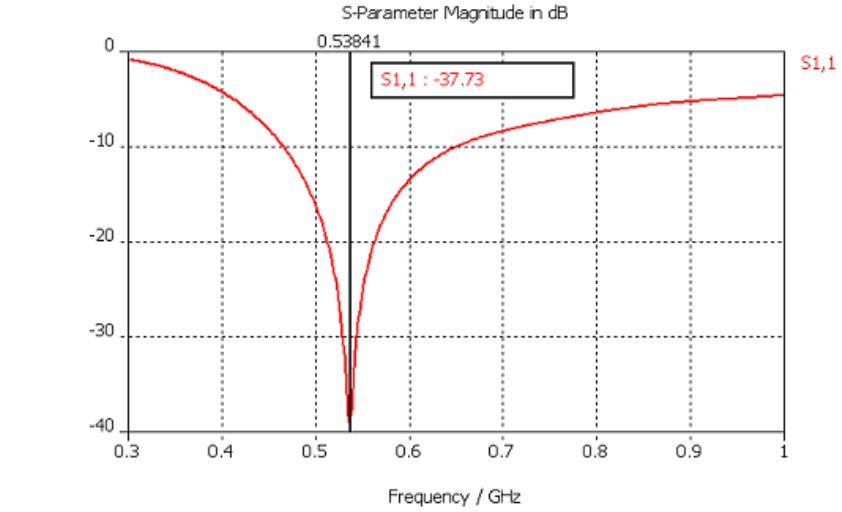

Figure 1.46: The return loss for the array backed by a ground plane and the distance to the ground plane is 85 mm, a capacitor with $C = 0.12732 \times 2$ pF is used to connect the ends of dipole elements.

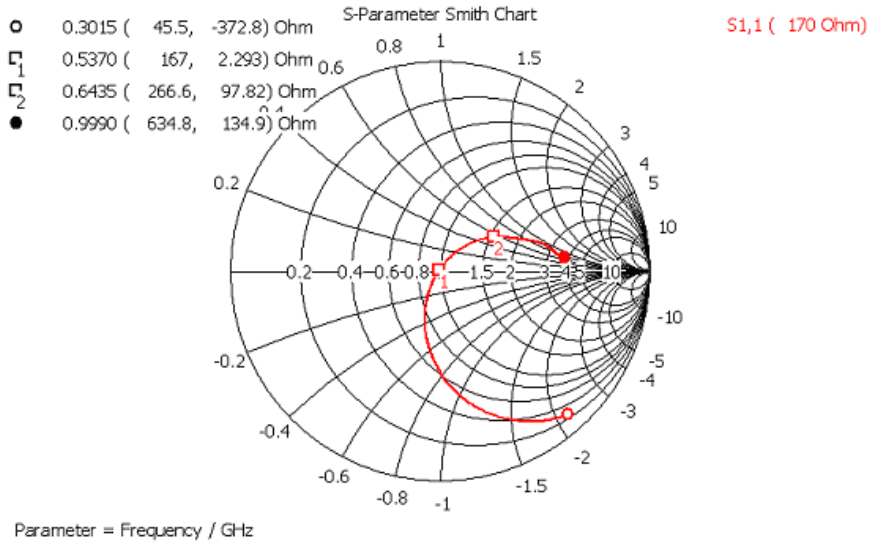

Figure 1.47: The Smith chart for the array backed by a groundplane and the distance to the groundplane is 85 mm, a capacitor with $C = 0.12732 \times 2$ pF is used to connect the ends of dipole elements.

1.4.2 Munk Dipole Array

One approach to make the bandwidth broader is to fill the space between the dipole array and the groundplane with higher dielectric constant material than free space. Furthermore, the greater bandwidth can be obtained by putting layers of dielectric slabs over the dipole elements. We first put one layer as a start. The dipole element is shown in Figure 1.48. The dipole array with one layer of dielectric material on the top is shown in Figure 1.49. The return loss and Smith chart for the element in the infinite dipole array with one layer of slab is shown in Figure 1.50 and Figure 1.51. The dipole element radiation pattern is shown in Figure 1.52 when the array is scanned to the boresight.

Figure 1.48: The dipole element without dielectric material layers, the capacitance at the ends to provide field continuity between the elements.

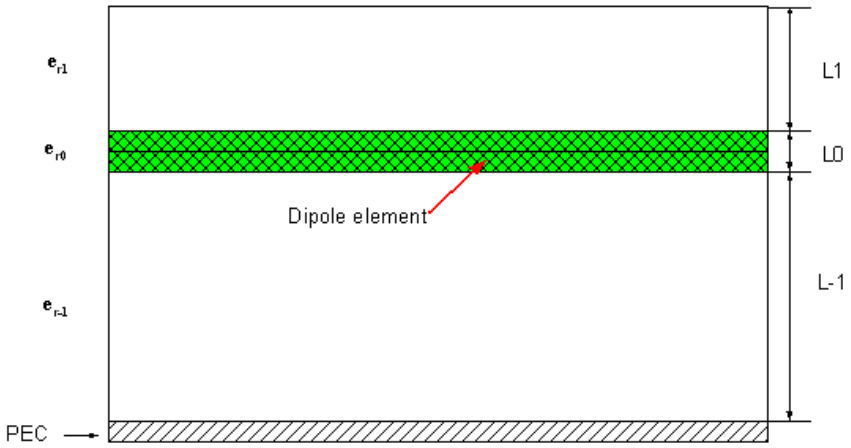

Figure 1.49: The dipole array with single layer of dielectric material on the top, side view.

With one layer of dielectric material on the top of the dipole array, the return loss performance is optimised by changing the thickness of the dielectric material. The thin dielectric underwear (to isolate the dipole element from other layers) is given with the thickness

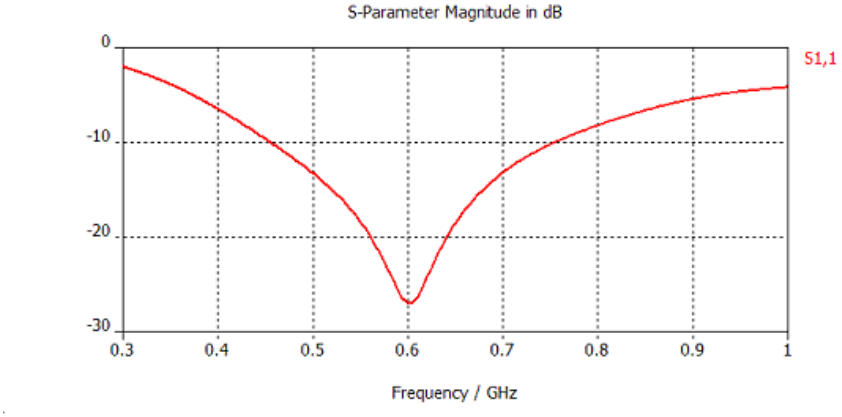

Figure 1.50: Return loss for the dipole array with a single layer of dielectric material on the top.

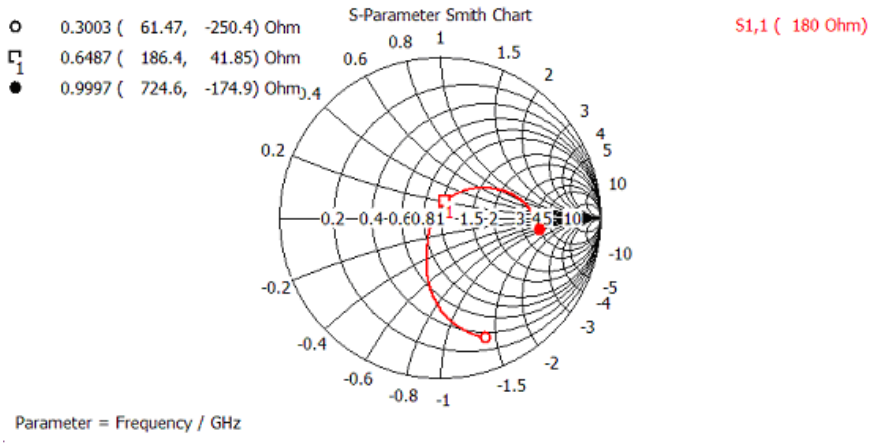

Figure 1.51: Smith chart for the dipole array with single layer of dielectric material on the top.

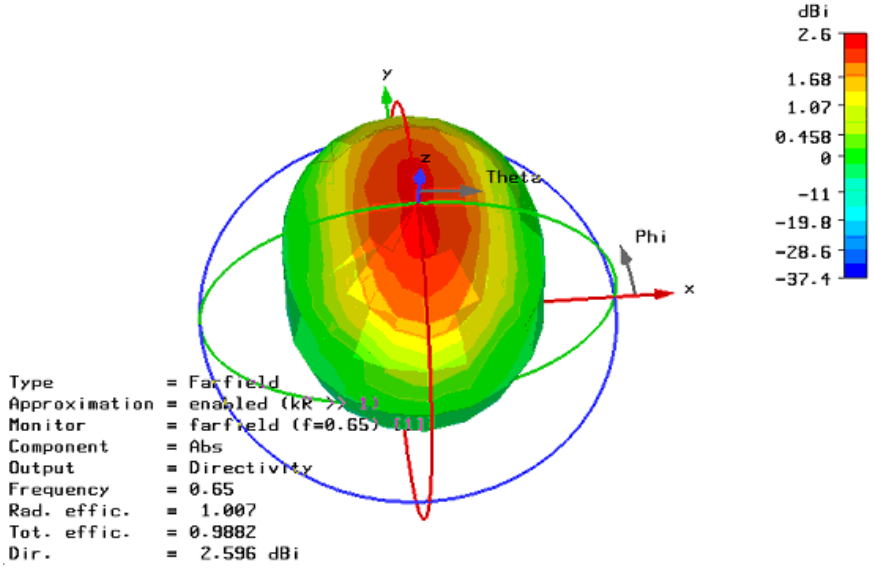

Figure 1.52: The dipole element radiation pattern when the array is scanned to the boresight.

of $L_0 = 60$ mils with $\epsilon_{r0} = 3$. This is shown in the Figure 1.53.

1.4.3 Munk Slot Elements Array

According to the complementary principle, slot elements can be introduced. Slot elements exhibit broader pattern than dipole elements, hence it is a desired candidate for arrays with wide scan angle (over 45°). Dielectric layers are needed to provide impedance stability over a range of scan angles. Inductance should be added between elements to provide field continuity. However, the inductance is hard to implement between the slots on a metal plate. Previous studies show that a taper slot structure is inductive when the plate is thin. Therefore, narrower slots are cut between the slot elements. The width of the "connection" slots can be adjusted to "tune" the value of inductance between the adjacent elements. This is shown in Figure 1.54. The side view of the slot elements array is shown in Figure 1.55.

The width of the slot and distance from the slot array to the groundplane are determined by parametric sweeping in CST MWS in an infinite array environment. The dependence of the return loss performance for the slot elements on the slot width and distance to the ground plane are shown in Figure 1.56 and Figure 1.57. They indicate the slot must have a reasonable width and a large separation distance from the groundplane in order to work in the high end of the frequency band.

The slot element with two layers of dielectric material on the top is simulated. At the centre frequency $f = 650$ MHz, the free space wavelength is $\lambda = 461$ mm. Initially dielectric material is assumed to fill the space between the groundplane and the slot elements, the space to the groundplane is $L\_1 = 0.137\lambda = 63$ mm, the dielectric constant for the material is assumed $\epsilon_{r1} = 1.7$. The first layer above the slot elements is used with material

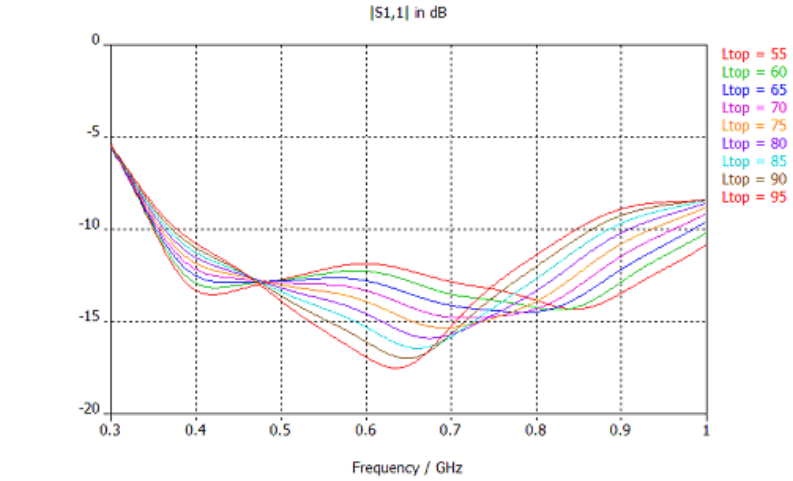

Figure 1.53: The dipole array with one layer of dielectric material above of different thickness, $\epsilon_{r1} = 1.5$, the impedance is normalised to 135 ohms.

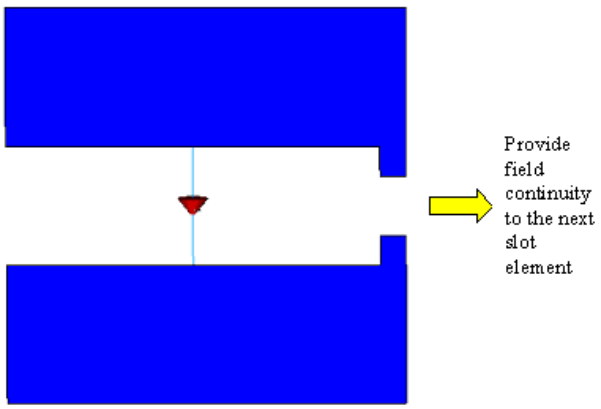

Figure 1.54: The slot element "unit cell" without dielectric material layers. The top view.

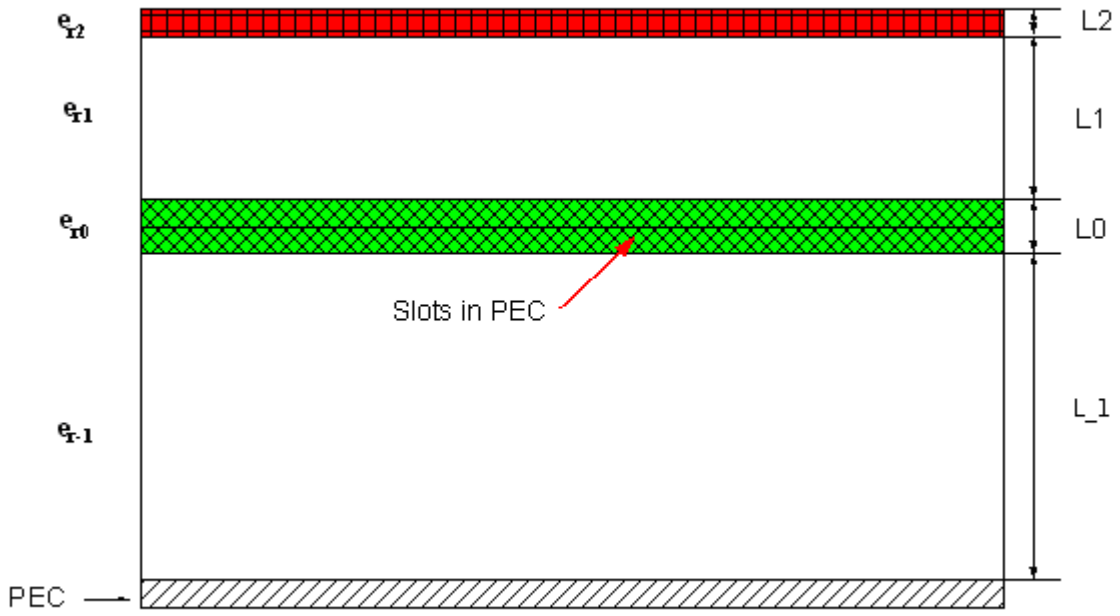

Figure 1.55: The slot element with two layers of dielectric material on the top, side view.

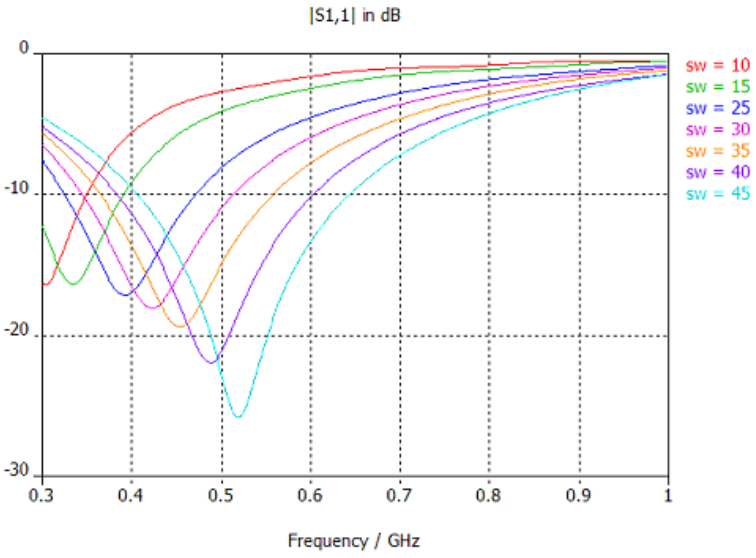

Figure 1.56: The return loss of the slot elements array, sw is the width of the slot. The impedance is normalised to 260 ohms.

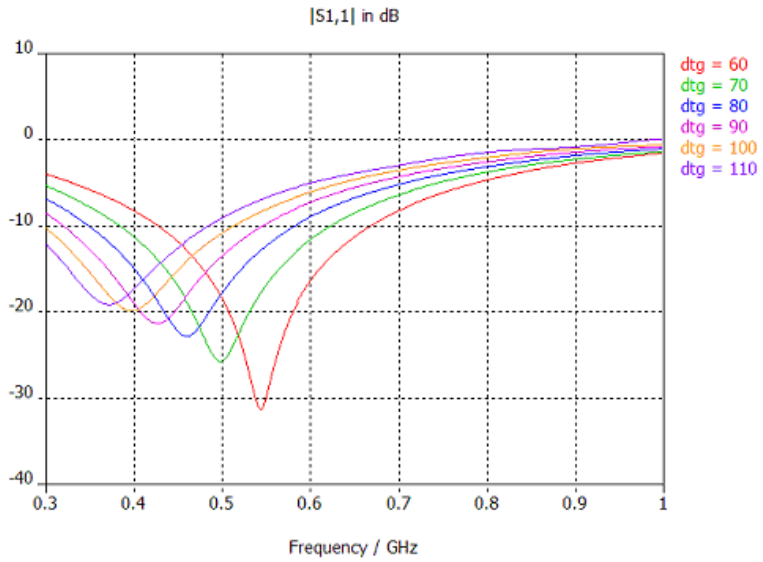

Figure 1.57: The return loss of the slot elements array, dsg is the distance from the slot elements array to the groundplane. The impedance is normalised to 260 ohms.

of $\epsilon_{r1} = 1.3$, the thickness of the first layer is $T_1 = 0.093\lambda = 43$ mm. The second layer is a very thin material with $\epsilon_{r2} = 3$ and thickness of $T_2 = 30$ mils $= 0.762$ mm. The size of the "connection slot" significantly affects the array performance and this is shown in Figure 1.58. The ratio between the width of the connection slot to the width of the slot element is defined as sf. The bandwidth increases when sf becomes larger, however the bandwidth stop increasing when sf is greater than 1, where it has the same or larger width as the slot element.

The return loss performance and the Smith Chart for the slot element when the "connection slot" is given half the width of the slot element are shown in Figure 1.59 and Figure 1.60.

Then the inductive "connection slot" is made wider to increase the inductance between the elements, the performance is shown in Figure 1.61 and Figure 1.62 when the "connection slot" has the width of three quarters of the width of the slot element.

The slot element array with wider inductive "connection" slot between the adjacent elements shows better performance. This is understandable for they provide better field continuity between the slot elements. The radiation pattern for the slot element in an infinite array is shown in Figure 1.63 in E-plane and Figure 1.64 in H-plane when the array is scanned to the boresight direction. It is noted the element pattern will change when the array is scanned to any other directions.

The dielectric constant of the second layer is changed from $\epsilon_{r2} = 3$ to $\epsilon_{r2} = 4$, the performance has a slight change. It is assumed that the thin second layer material has no significant effect on the overall bandwidth improvement. The height of the second layer material is then changed between 30 mils (0.762 mm) to 900 mils (22.86 mm). The return loess performance for the sweeping is shown in Figure 1.65.

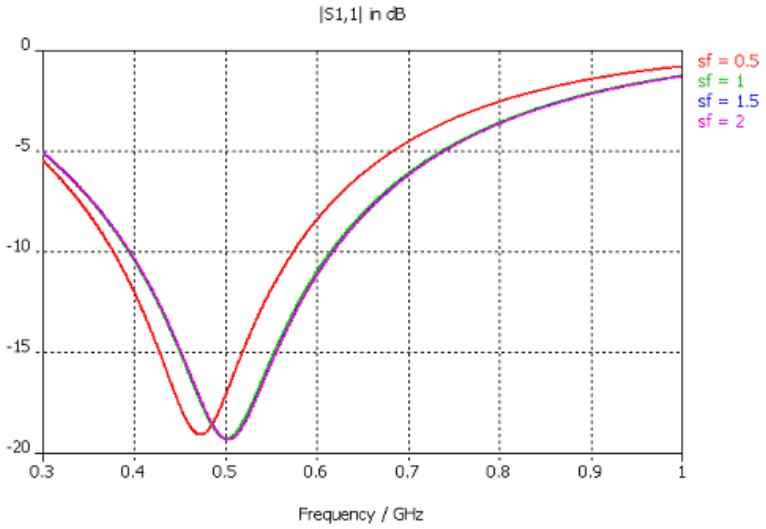

Figure 1.58: The return loss for different widths of "connection" slot with respect to the width of the slot element. sf is the factor of the width of the "connection slot" with respect to the width of the slot element.

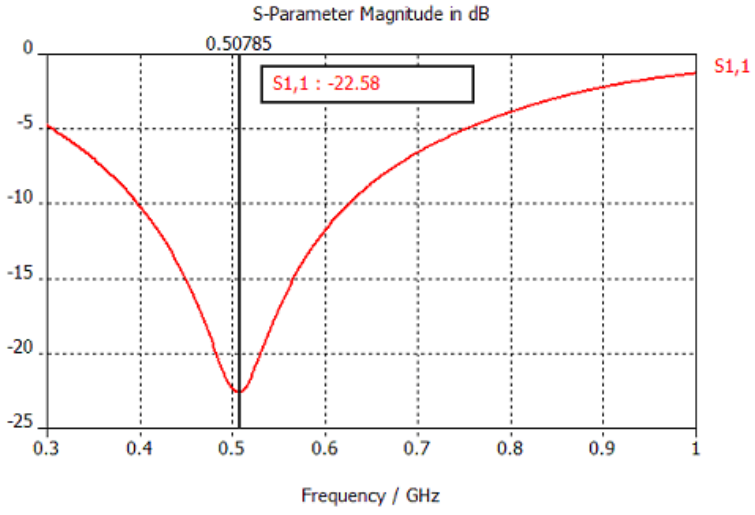

Figure 1.59: The inductive "connection" slot is half the width of slot element.

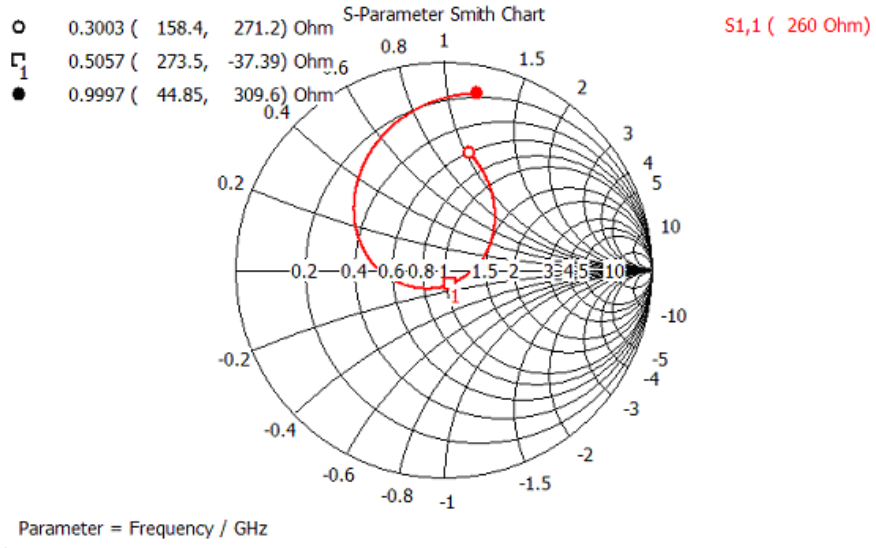

Figure 1.60: Smith chart for the slot elements array with the inductive "connection" slot half the width of slot elements.

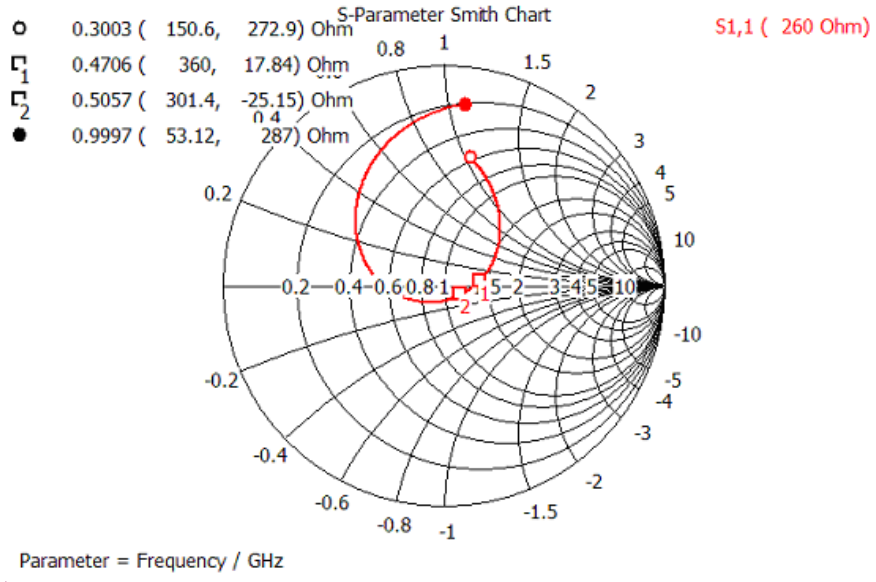

Figure 1.61: Slot elements array with the "connection" slot three quarters of the width of the slot element.

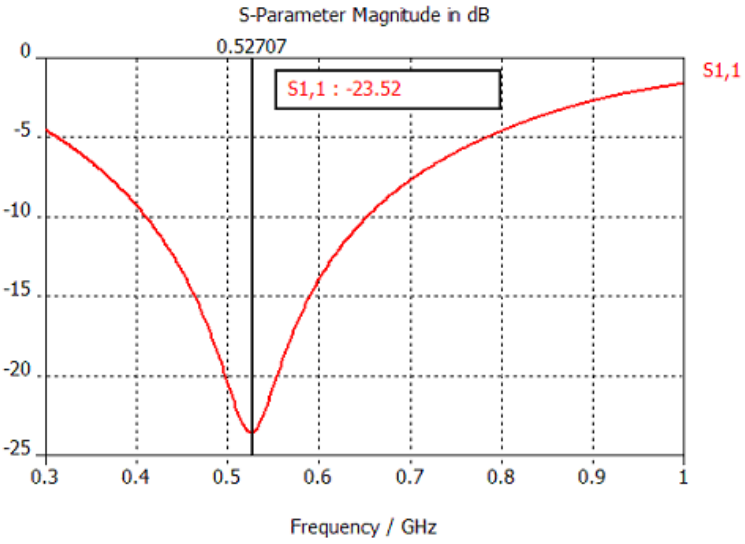

Figure 1.62: Slot elements array with the "connection" slot three quarters of the width of the slot element.

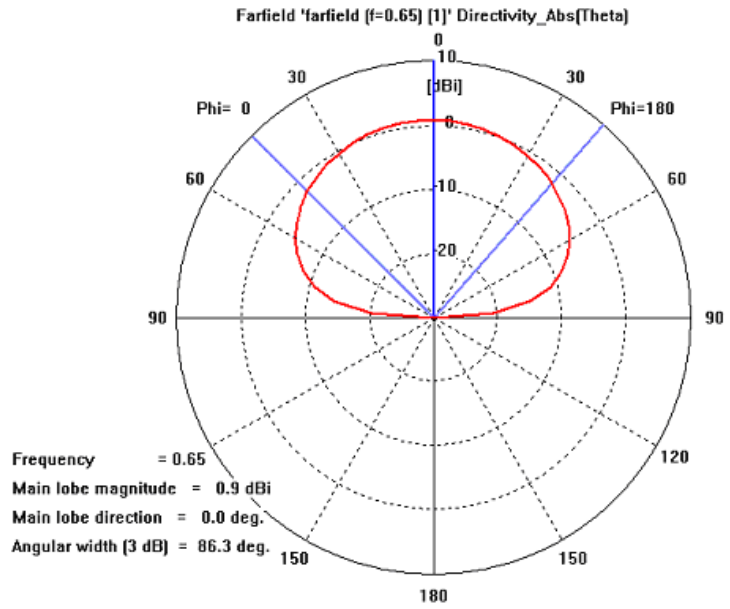

Figure 1.63: E-plane slot element radiation pattern for boresight scan at centre frequency $f = 650$ MHz.

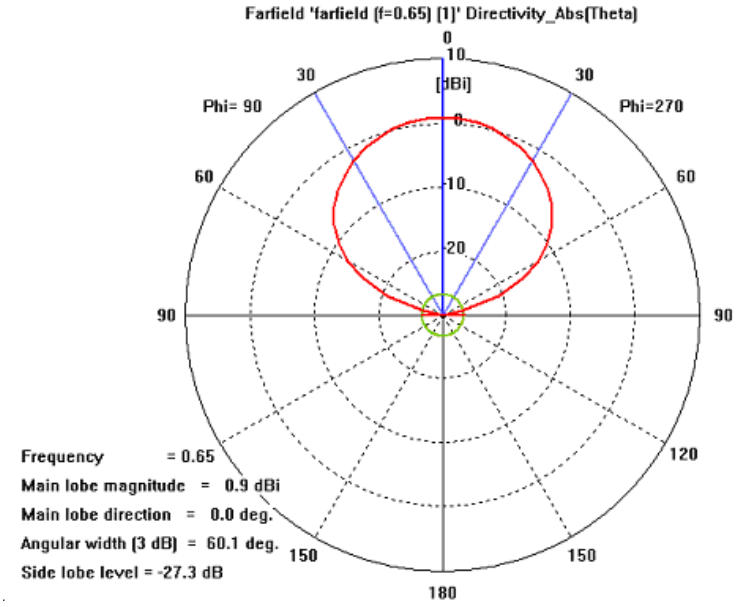

Figure 1.64: H-plane slot element radiation pattern for boresight scan at centre frequency $f = 650$ MHz.

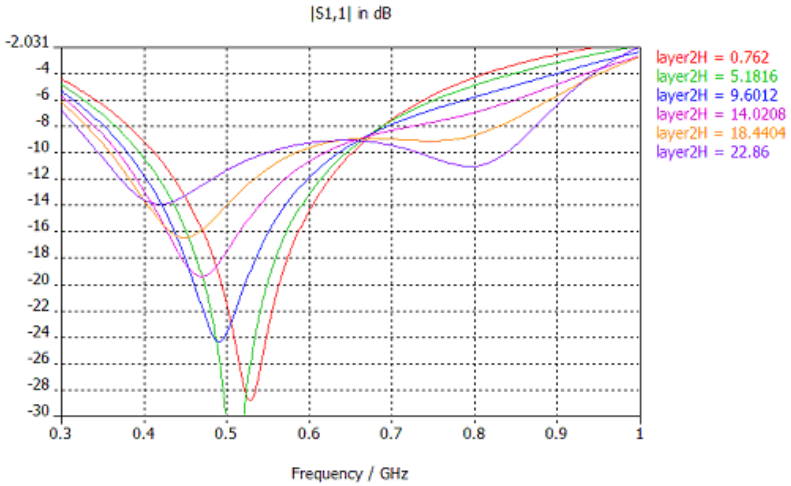

Figure 1.65: The array return loss performance changes with the thickness of the second layer of dielectric material on the top.

It implies that the greater thickness of the second layer, the wider bandwidth available, hence the thickness of the second layer is changed to $L_2 = 1200$ mils $= 30.48$ mm, the Smith chart and the return loss for this scenario is shown in Figures 1.66 and 1.67.

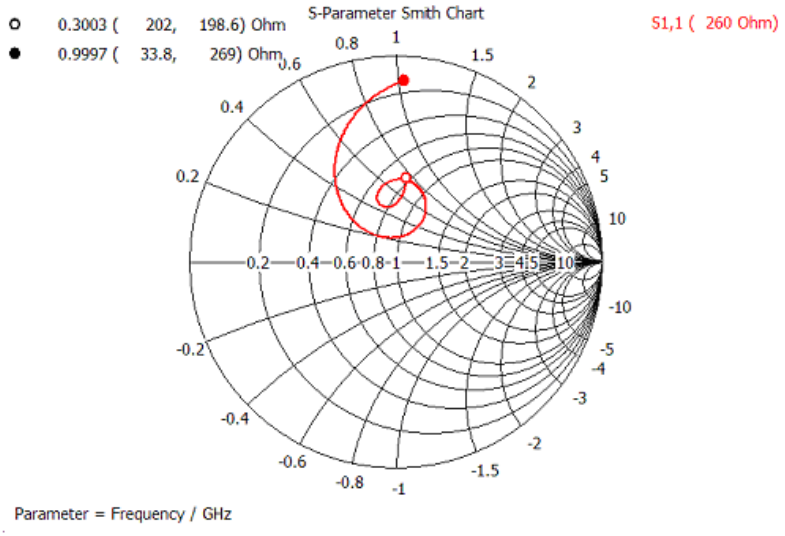

Figure 1.66: Smith chart for the slot element array, $L_1 = 0.093\lambda = 42.9$mm, $L_2 = 1200$ mils $= 30.48$mm, $\epsilon_{r1} = 1.3$, $\epsilon_{r2} = 4$.

Incrementing L_2 from 900 mils to 1200 mils merely shifts the operational bandwidth towards the lower frequency end, however the overall bandwidth stays the same (350 MHz to 850 MHz). In addition, the middle lobe shows an increasing trend. The thickness of the first layer of dielectric material L_1 is further optimised by giving different values, this is shown in Figure 1.68, middle lobes are minimised when $L\_1 = 58$ mm.

The return loss performance for the slot element array with the thickness of the first layer $L\_1 = 53, 58,$ and 63 mm is shown in Figure 1.69.

A long slot array presents ultrawide-band properties fed by equally spaced sources [NL05]. The Munk slot antenna becomes an infinite long slot structure when the "connection" slot has the same width as the slot element. For an infinitely long slot structure as shown in Figure 1.70, the return loss and the Smith chart is shown in Figure 1.71 and Figure 1.72. This is based on the following assumptions, $L\_1 = 75$ mm, $L1 = 58$ mm, $\epsilon_{r1} = 1.3$, $\epsilon_{r2} = 4$. It is difficult to build a dual-pol array with this structure.

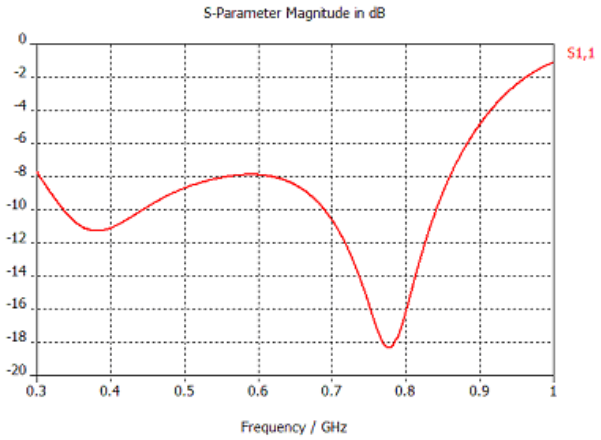

Figure 1.67: Return loss for the slot element array, $L_1 = 0.093\lambda = 42.9$mm, $L_2 = 1200$ mils $= 30.48$mm, $\epsilon_{r1} = 1.3$, $\epsilon_{r2} = 4$. λ is the wavelength for free space at centre frequency $f = 650$ MHz.

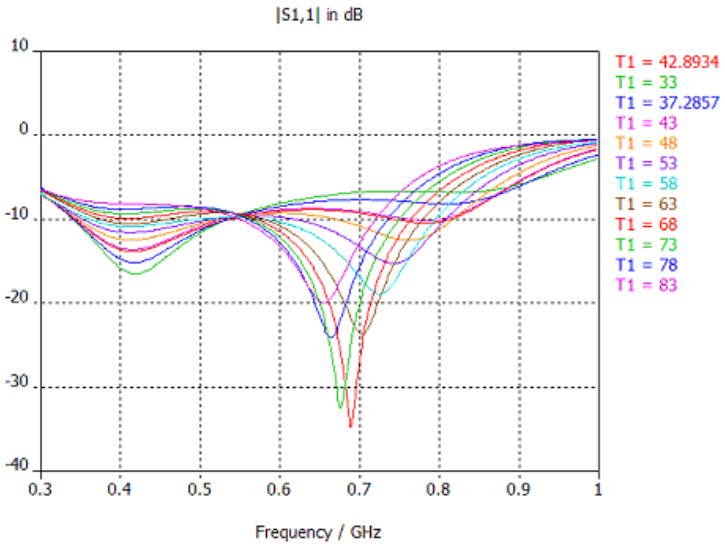

Figure 1.68: The return loss performance of the slot element array changes with the thickness of first layer dielectric material on the top, $\epsilon_{r1} = 1.3$; The second layer on the top is given $\epsilon_{r2} = 4$ and the thickness of $L_2 = 900$ mils $= 22.86$ mm. The thickness for the underwear layer is $L_0 = 60$ mils with $\epsilon_{r0} = 2.2$. The impedance is normalised to 260 ohms.

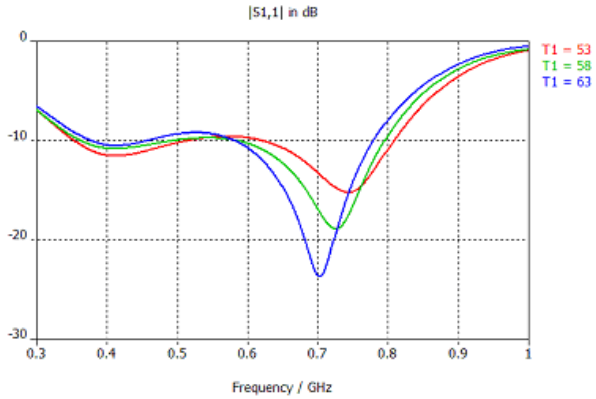

Figure 1.69: The return loss of the slot element array with the thickness of the first layer of $L\_1 = 53,\ 58,$ and 63 mm, $\epsilon_{r1} = 1.3$, the width of the slot 46.1 mm.

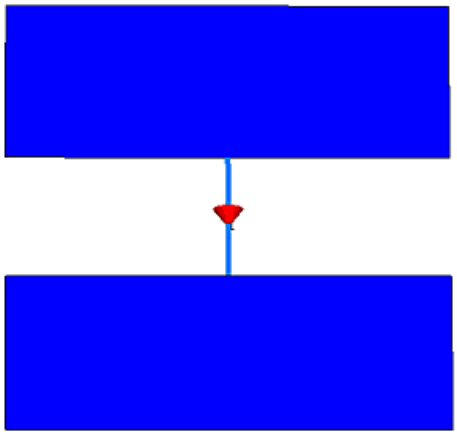

Figure 1.70: The infinite long slot structure, two layers of dielectric material on the top are not shown.

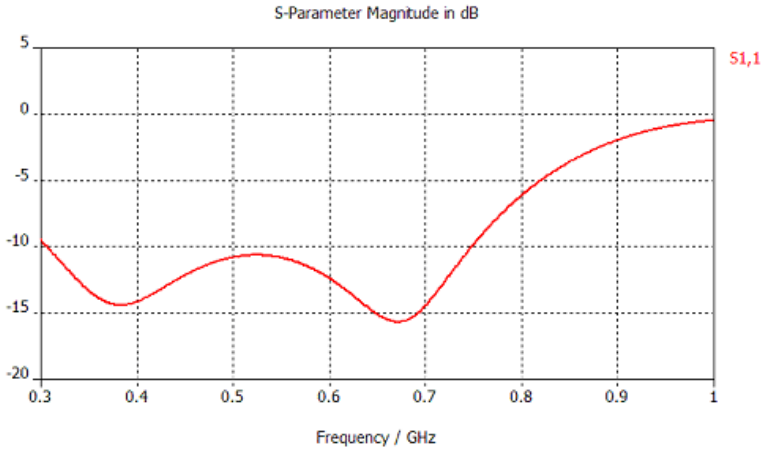

Figure 1.71: VSWR performance for the infinite long slot structure, two layers of dielectric material on the top of the slot elements, the distance from the groundplane is 75 mm.

The slot element is then made shorter as shown in Figure 1.73. Another element can be put perpendicularly to it to form the dual-pol array. The simulated results for an array with this structure are shown in Figure 1.74 and Figure 1.75.

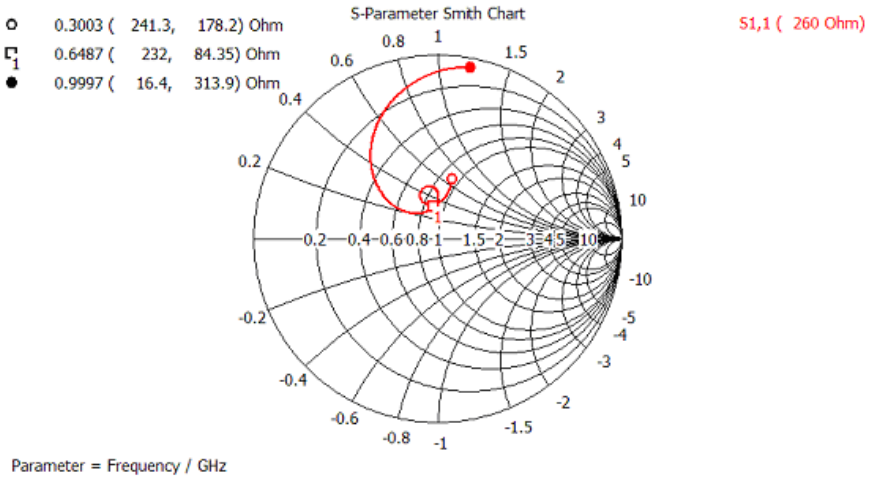

Figure 1.72: The Smith chart for the infinite long slot structure.

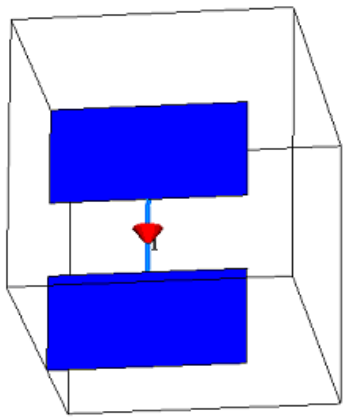

Figure 1.73: Dual-pol slot structure, the width of the slot is one-tenth of the lambda at the central frequency.

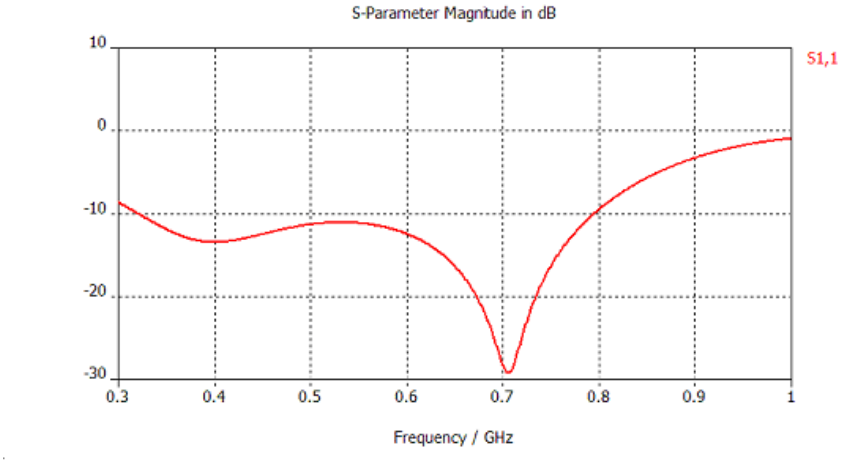

Figure 1.74: The return loss performance for the dual-pol slot structure.

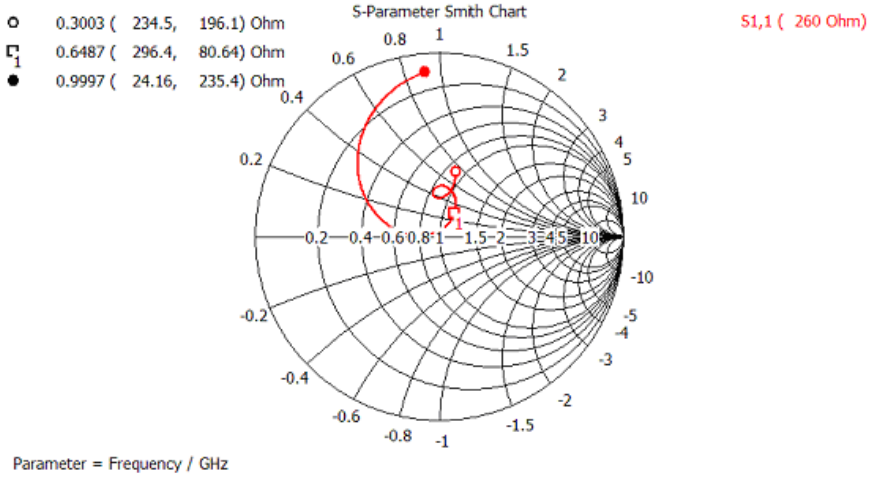

Figure 1.75: The Smith chart for the dual-pol slot structure.

1.5 Metal Tape Roll Antenna

The planar architecture of tapered slot element is constructed with pure metal. A single element works best when the length of the slotline is more than one wavelength and the height of the aperture is more than one-half wavelength at the lowest frequency. The aperture slotline formed by the infinite thin metal shows inductance characteristics. The impedance matching can be improved by giving a thickness to the metal plate. Initially, the metal plate has a thickness of 10 mm10. The structure for the single element is shown in Figure 1.76.

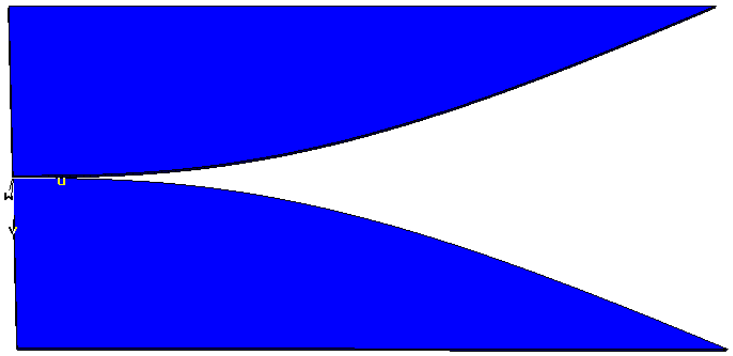

Figure 1.76: Metal flared slot antenna, the thickness of the plate is 10 mm. The length of slotline is 1100 mm, the height of the aperture is 550 mm.

The return loss performance and the Smith Chart for the single element are shown in Figure 1.77 and Figure 1.78. This element intends to cover the whole band from 0.3 GHz to 1 GHz.

The single metal flared slot antenna shows a very narrow radiation pattern in the E-plane, this is given in Figure 1.79 at the centre frequency $f = 0.65$ GHz.

A broader beamwidth can be achieved by reducing the aperture height to 250 mm, which is one-half wavelength at the frequency of $f = 600$ MHz. Accordingly the length of the slotline is reduced to 500 mm to maintain an identical radiation pattern in both E- and H- planes. The element can work in the low frequency band (from 300 MHz to 600 MHz) by using the coupling between the adjacent elements in a close-packed array. The array formed by this element backed by an infinite background shows resonances at frequency $f = 0.83$ GHz and $f = 1.02$ GHz. They are believed stemming from the higher order modes induced by the continuous metal plate structure. The element performance is shown in Figure 1.80 when the metal plate has the thickness of 10 mm and 15 mm. An inductive behaviour is seen from the Smith chart shown in Figure 1.81, for the thickness of the metal plate of 10 mm.

The metal plate is then cut into a "bunny-ear" shape as shown in Figure 1.82. The performance for this element in an infinite array is shown in Figure 1.83, Figure 1.84 and

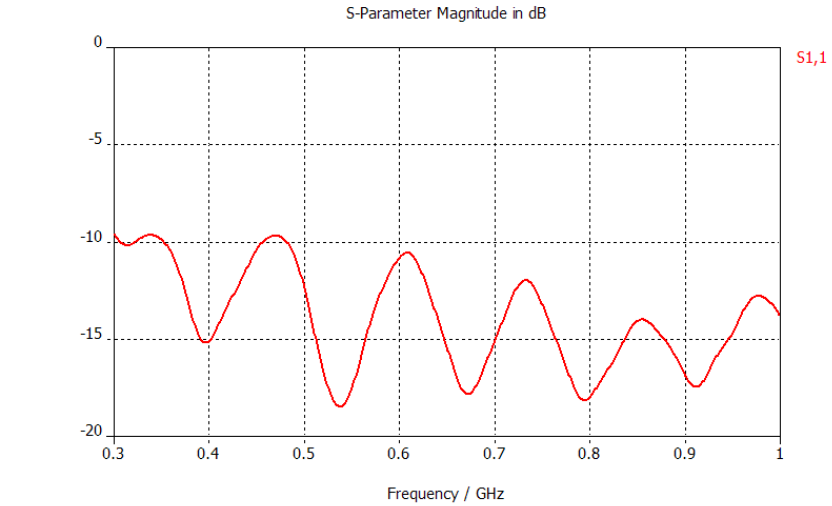

Figure 1.77: The return loss for a single metal flared slot antenna.

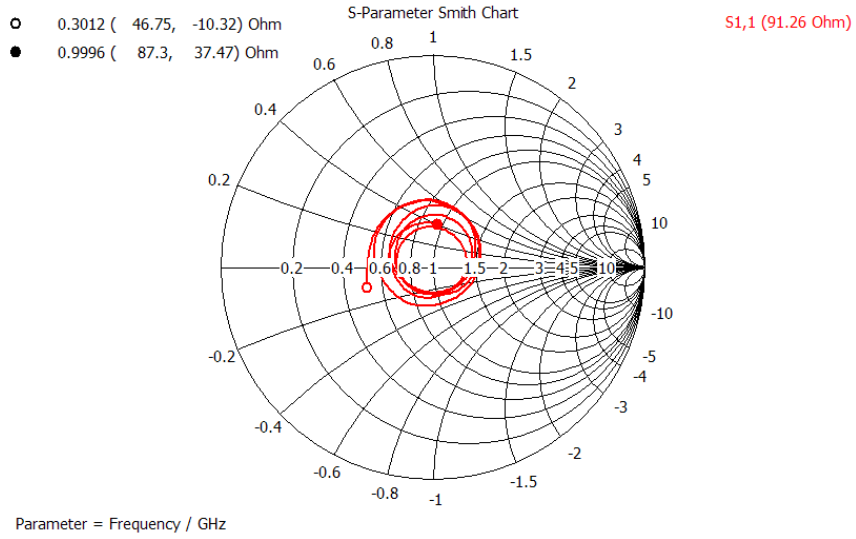

Figure 1.78: The Smith chart for the metal flared slot antenna.

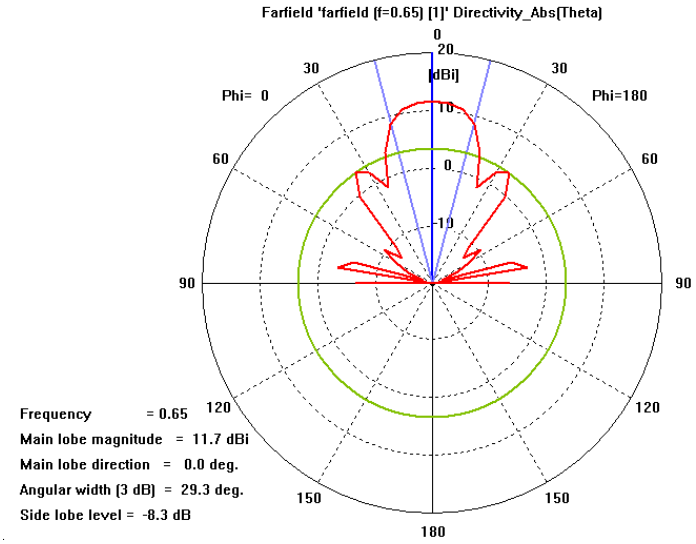

Figure 1.79: The radiation pattern in the E-plane at the centre frequency $f = 0.65$ GHz. The single flared tapered slot antenna.

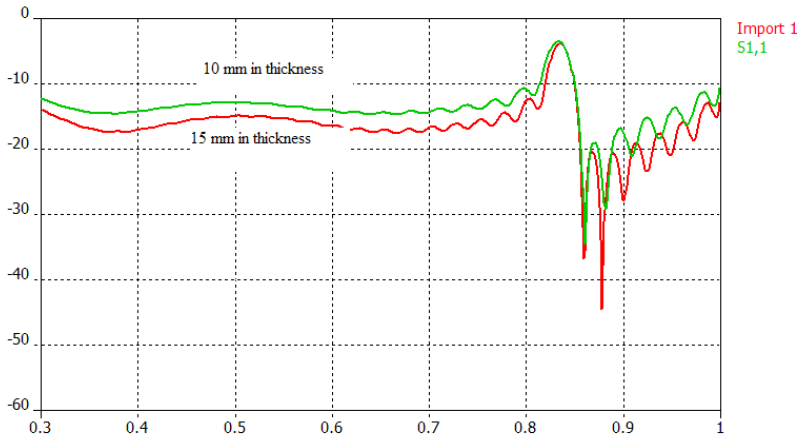

Figure 1.80: The return loss for the tapered slot antenna in an infinite array, the height of the aperture is 250 mm, the length of the slotline is 500 mm. The metal plate is given with different thicknesses.

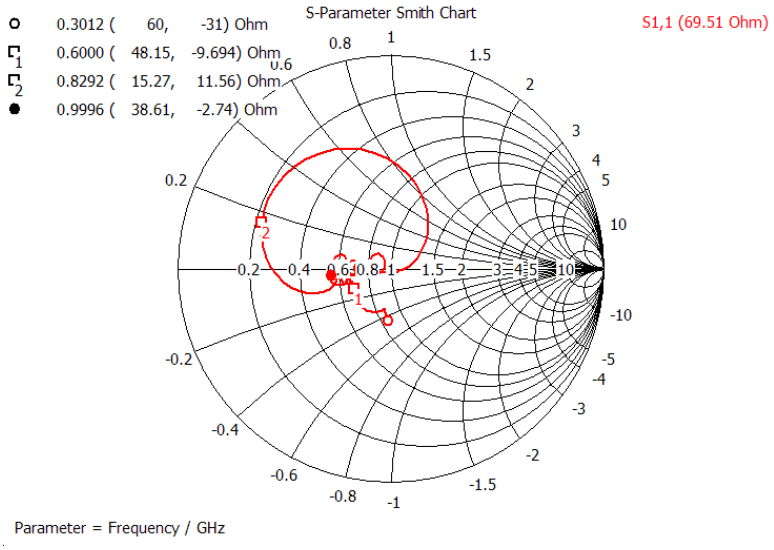

Figure 1.81: The Smith chart for the element in an infinite array with aperture height 250 mm, the length of the slotline 500 mm, and thickness of the metal board of 10 mm.

Figure 1.85. This shape brings some backward radiation as shown in Figure 1.85. A transition section is needed to enhance the forward gain and a groundplane can then be introduced.

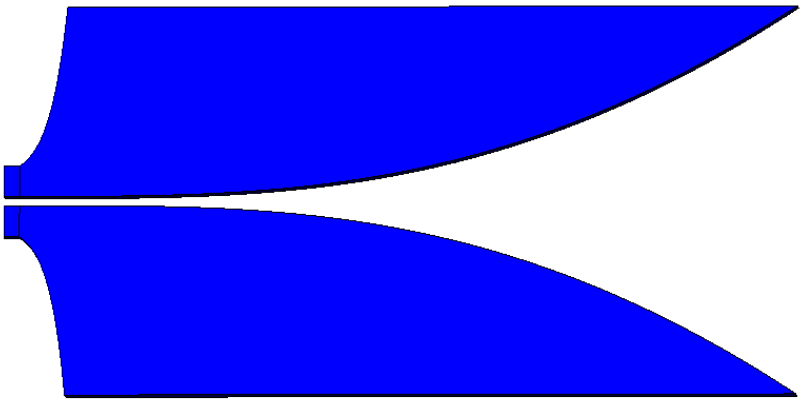

Figure 1.82: The metal plate is cut into a bunny ear shape.

1.5.1 Metal Tape Roll

The continuous metal planar structure is heavy. It is also noticed that the surface current is concentrated along the tapered slotline and the edge of the metal plate. Therefore, the structure with only the edge part of the plate is initiated. The advantage of this structure is that it can be built by rolling a metal tape into the tapered slotline profile and it has low wind resistance.

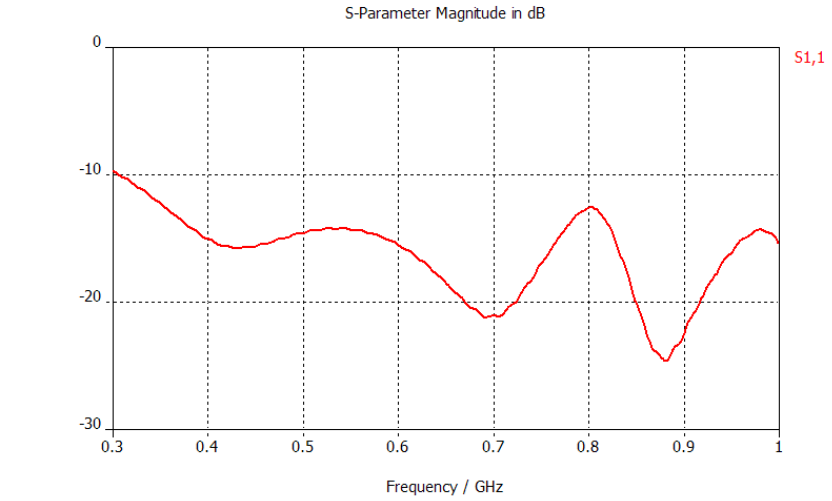

Figure 1.83: The return loss performance for the infinite array formed by the bunny-ear shape element.

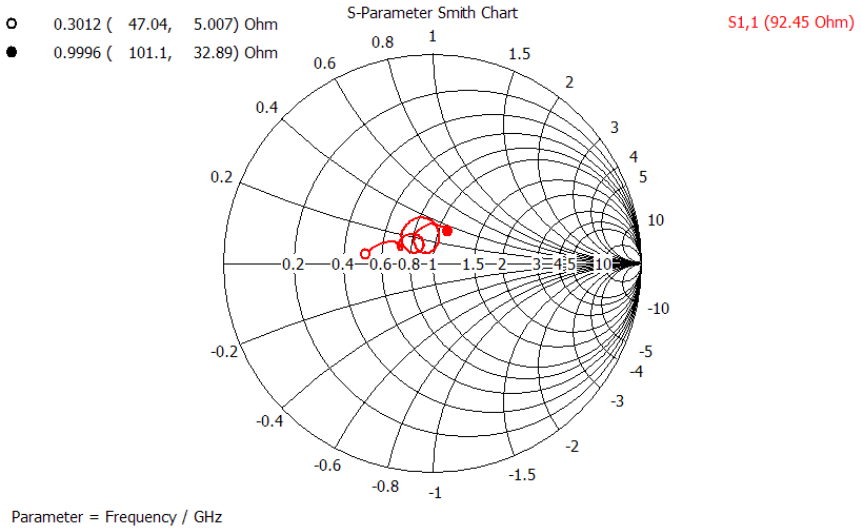

Figure 1.84: The Smith chart for the infinite array with bunny-ear shape element.
Untitled

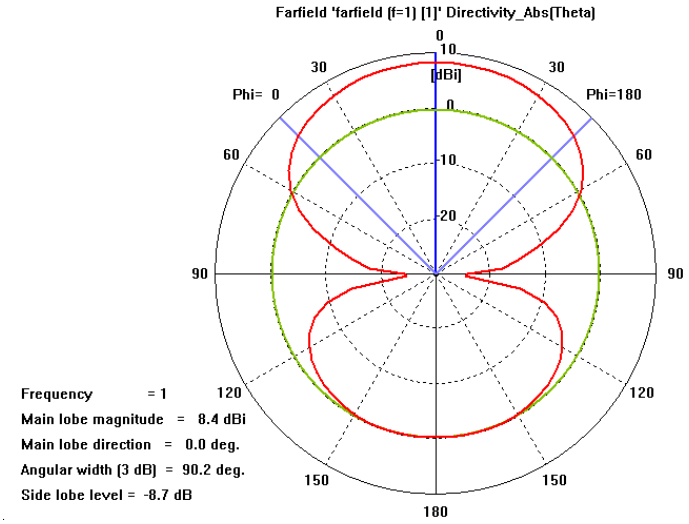

Figure 1.85: The radiation pattern in the E-plane for the metal plate of bunny-ear shape.

The shape as a photo frame is built initially as shown in Figure 1.86. It has a slotline length of 55 cm, the height of the tapered aperture is 50 cm. The return loss performance and the Smith chart for a single element is shown in Figure 1.87 and Figure 1.88, two lobes in the middle of the operational band is observed.

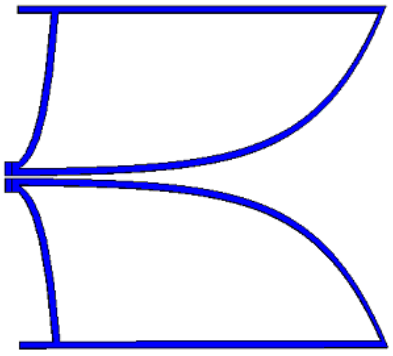

Figure 1.86: Metal strip frame antenna with the geometry of 500 mm $(H) \times 550$ mm (L).

The metal strip roll is optimised further to achieve a better impedance matching. The structure is shown in Figures 1.89. The return loss and the Smith chart for the element backed by a groundplane are shown in Figures 1.90 and 1.91. Future research will involve in simulating the metal strip roll antenna in an array environment.

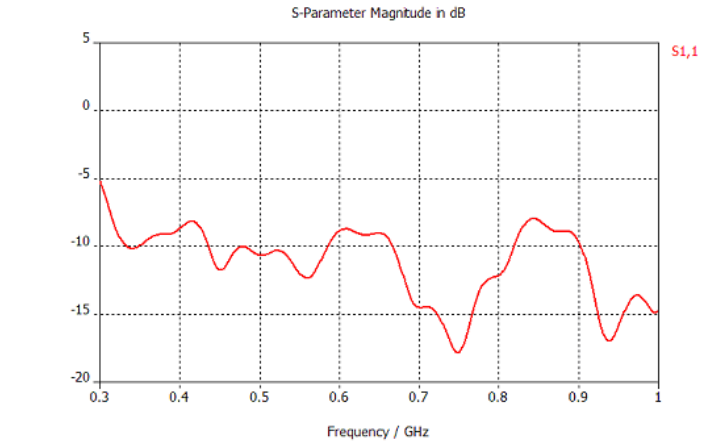

Figure 1.87: Return loss for the metal strip frame antenna of the size 500 mm $\times$ 550 mm.

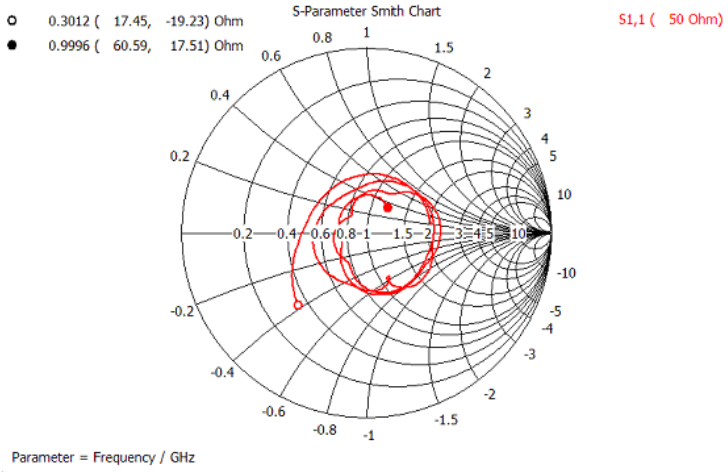

Figure 1.88: Smith chart for the metal strip frame antenna of the size 500 mm $\times$ 550 mm.

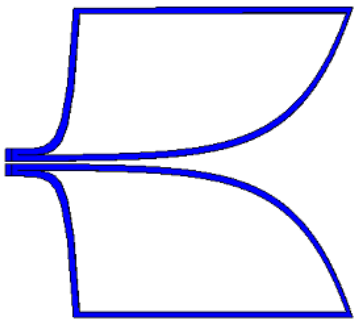

Figure 1.89: Metal strip frame antenna with the size of 500 mm (H) $\times$ 550 mm (L).

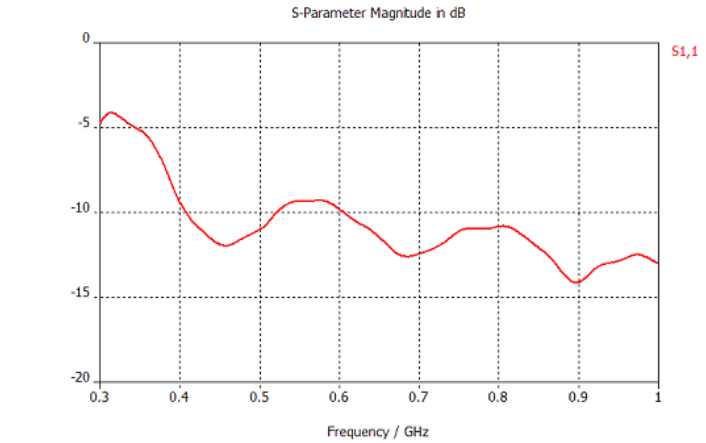

Figure 1.90: Return loss for the Metal strip frame antenna with the size of 500 mm × 550 mm.

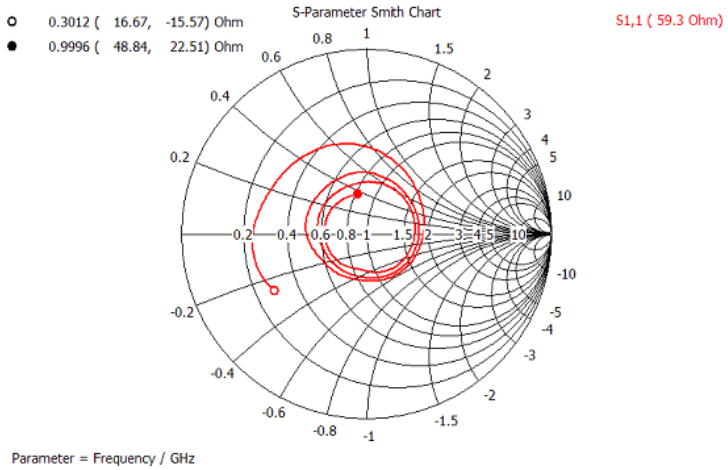

Figure 1.91: Smith chart for the metal strip frame antenna with the size of 500 mm × 550 mm.

Bibliography

[CS00] T-H. Chio and D.H. Schaubert. Parameter study and design of wide-band dual-polarized tapered slot antenna arrays. *IEEE Trans. Antenna Propagat.*, 48(6):879–886, June 2000.

[HCS00] H. Holter, T-H. Chio, and D. Schaubert. Elimination of impedance anomalies in single- and dual-polarized endfire tapered slot phased arrays. *IEEE Trans. Antenna Propagat.*, 48(1):122–124, January 2000.

[LFH74] L.R. Lewis, M. Fasset, and J. Hunt. A broad-band stripline array element. *IEEE Int. Symp. Antennas Propagat.*, pages 335–337, 1974.

[LLK03] J.J. Lee, S. Livingston, and R. Koenig. A low-profile wide-band (5:1) dual-pol array. *IEEE Antennas And Wireless Propagat. Letters*, 2:46–49, 2003.

[Mun03] B.A. Munk. *Finite Antenna Arrays and FSS*. Wiley, 2003.

[NL05] A. Neto and J.J. Lee. *"Infinite Bandwidth" Long Slot Array Antenna*, volume 4, pages 75–78. 2005.

[YKK+84] K.S. Yngvesson, T.L. Korzeniowski, Y.S. Kim, E.L. Kollberg, and J.F. Johansson. The tapered slot antenna – a new integrated element for millimetre-wave applications. *IEEE Trans. Microwave Theory Tech.*, MTT-37:365–374, February 1984.

Chapter 2

Simulation Performance

This chapter concentrates on the large scale computational electromagnetics which simulates the wave propagation in the vicinity of the Vivaldi antenna array elements. First the architectures of the supercomputer Bull system at the University of Manchester (called Horace) and the IBM BlueGene/L at the University of Groningen in the Netherlands are presented. After discussing the current experience with these systems and highlighting their drawbacks a thorough analysis of the potential performance of these machines is made. A section on the HDF5 – a scientific data format which offers better means for storage of simulation data will conclude this chapter.

2.1 Horace

2.1.1 Architecture

Horace is a high performance computing system based in the Manchester Computing facility at the University of Manchester. It consists of 192 processor cores based on the Bull Itanium 2 architecture. The overall amount of processor cores is spread between 24 compute nodes. Each of these nodes includes 4 Itanium 2 Montecito Dual Core 1.6 GHz processors with 8 MB of cache per processor. This means every Horace compute node offers 8 cores for computation. There are 16 GB of RAM and 512 GB of scratch disk space available for each node. There are 4 special purpose nodes have high memory configuration of 32 GB of RAM. All 24 compute nodes are connected by a single rail Quadrics QsNetll (elan4) interconnect. The whole system has a 10 TB large total filestore. Figure 2.1 represents the general architecture of a single computing node in Horace.

2.1.2 Drawbacks

As expected with supercomputers the low-throughput is the issue. To have jobs processed without significant waiting time, only 2 computing nodes, which refer to 64 processors and 32 GB of operating memory, were requested. The next drawback of the Horace architecture is a weak I/O mechanism.

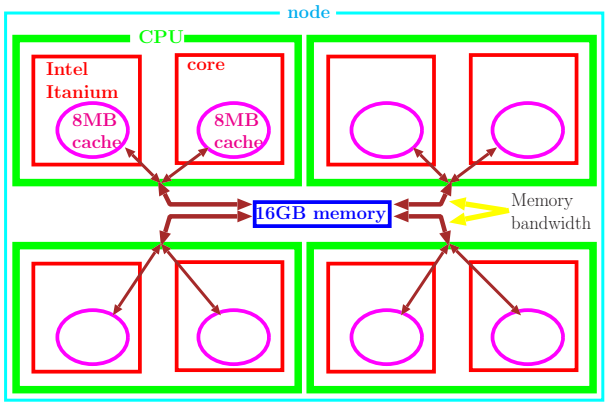

Figure 2.1: Computing Node Architecture in Horace

2.1.3 Potential Performance

Two series of experiments were conducted on Horace to estimate the system's potential performance. The first series included the simulation of a single Vivaldi antenna element. This simulation was conducted for 5000 timesteps and 16681707 grid points, since one antenna element occupies $189 \times 467 \times 189 = 16681707$ space grid points. All 6 electromagnetic field values E_x, E_y, E_z, H_x, H_y and H_z for the complete grid space were output into files. These real-world experiments were run on 2 computing nodes (16 processor cores) with 32 GB of operating memory. Refer to the section called "Single Vivaldi Antenna Element" below for further details about this series of experiments.

The second series was comprised of 6 experiments for various cubic space grid dimension sizes: 150, 250, 350, 450, 550 and 650 points. All experiments in this series were conducted for 100 simulation timesteps. Only E_z field values for the whole grid space were output into files. The same hardware resources on Horace were used to perform the second series of experiments – 2 computing nodes and 32 GB of RAM. Detailed analysis and discussion of this series could be found in the section named "Scientific Probing".

Single Vivaldi Antenna Element Running the simulation for a single Vivaldi antenna element allowed to estimate the potential operating memory usage. According to the Horace command line utility `bjobs -l` the amount of RAM used for this task was 1.768 GB. This means the amount of memory required to store one space grid point for the simulation is $1.768 \text{ GB} \,/\, 16681707 \text{ points} = 1.06 \times 10^{-7}$ GB. Knowing the amount of memory required to store a single grid point and the overall amount of RAM available to each computing node allows drawing further assumptions. The potential maximum dimension size for a cubic space grid that could be efficiently calculated on the Horace system equals to $\sqrt[3]{\frac{32 \text{ GB}}{1.06 \times 10^{-7} \text{ GB}}} \approx 670$ points. Another interesting result is a prediction of the overall amount of antenna elements that could be calculated on Horace without using the disk swap area. This equals to $670^3/16681707 \approx 18$ antenna elements.

The simulation produces one file per timestep per processor. Currently the output is produced in ASCII form and consists of 9 field records. The fields of a single file record are the x, y and z coordinates, and H_x, H_y, H_z, E_x, E_y and E_z electromagnetic field values. Each file produced was approximately 200 MB large. The

amount of disk space required to accommodate the total simulation data would be 5000 timesteps $\times$ 8 processors $\times$ 200 MB $=$ 7.6294 TB. And this is not yet the maximum amount of information that could be stored in an output file.

It took approximately 6 minutes to output one file for a time step on each processor. The complete calculation of 5000 timesteps would have required 5000 files $\times$ 6 minutes $=$ 500 hours $\approx$ 21 days.

Scientific Probing Figure 2.2 presents the total memory requirements for the simulation. The theoretical memory usage was estimated based on the data obtained from the simulation of a single Vivaldi antenna mentioned earlier. A series of experiments for the grid dimension sizes of 150, 250, 350, 450, 550 and 650 resulted in the experimental curve on the Figure 2.2. It is important to notice that theoretical assumptions represent the worst-case memory usage scenario. The experiments show that real memory demands are less intensive and it would be possible to simulate a cube with the grid dimension larger than 670 points and hence accommodate more than 18 antenna elements. The intersection of the theoretical and experimental curves is the value obtained from the single Vivaldi antenna simulation.

Figure 2.3 depicts the single output file size according to the grid dimension.

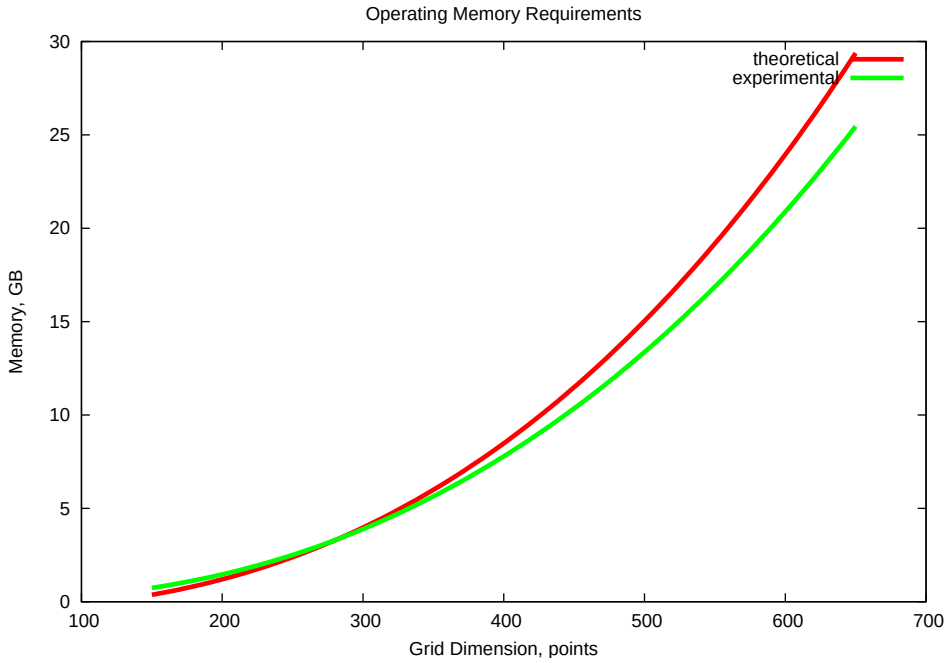

Figure 2.2: Operating Memory Requirements

Refer to Figure 2.4 to observe the total processing time of a single timestep according to grid dimension size. The processing time of a timestep is the summation of the field calculation and output production times for a particular timestep. The processing time was measured for a single CPU.

The processing time of 35 minutes for 550 and 58 minutes for 650 grid dimension sizes is high in comparison to 1 and 3 minutes for 150 and 250 dimension sizes. This significant increase of processing time might be caused by the weak I/O mechanism of Horace, which might not be suitable for the I/O intensive computations. Also similar to the IBM BlueGene/L (see 2.2.2) there might be less I/O nodes than the

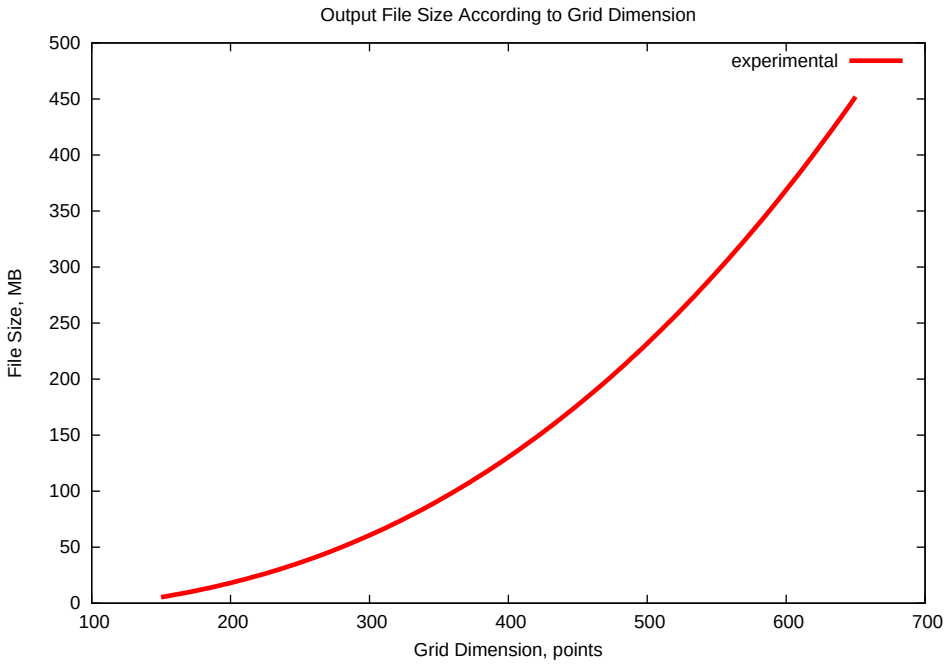

Figure 2.3: Output File Size According to Grid Dimension

computing nodes in Horace. At some point the I/O nodes might become highly overloaded. However this problem needs further investigation. A series of experiments should be conducted with and without I/O of electromagnetic values.

Figure 2.5 highlights the total time requirements for a complete simulation. Depending on the grid dimension size and hence the single timestep processing time the overall simulation time increases with the number of FDTD grid points. The theoretical curve's values were calculated from the experiment with a 150 dimension size. The experimental curve does not follow the theoretical one because of the 24 hours job running time limit in Horace. The experiments were successfully finished for 150, 250 and 350 grid dimension sizes. The 450, 550 and 650 were terminated by the Horace scheduling system, because they required more than 24 hours of simulation time.

2.2 IBM BlueGene/L

2.2.1 Architecture

IBM BlueGene/L (BGL) is a massively parallel supercomputer architecture developed by IBM and Lawrence Livermore National Laboratory (LLNL). The particular system intended for usage in our Frequency-Dependent Finite Difference Time Domain (FD-FDTD) simulation is the IBM BlueGene/L implementation for the Astron/Lofar project. This machine is based on the premises of the University of Groningen in the Netherlands. The Astron/Lofar system consists of 6 racks, where each rack includes 128 I/O nodes and 1024 compute nodes.

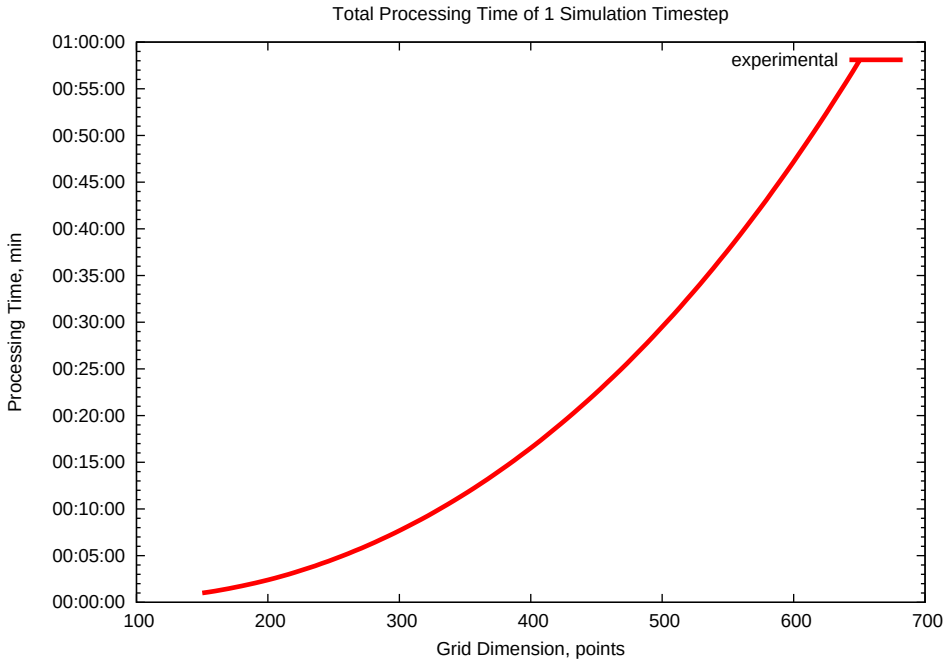

Figure 2.4: Total Processing Time of 1 Simulation Timestep

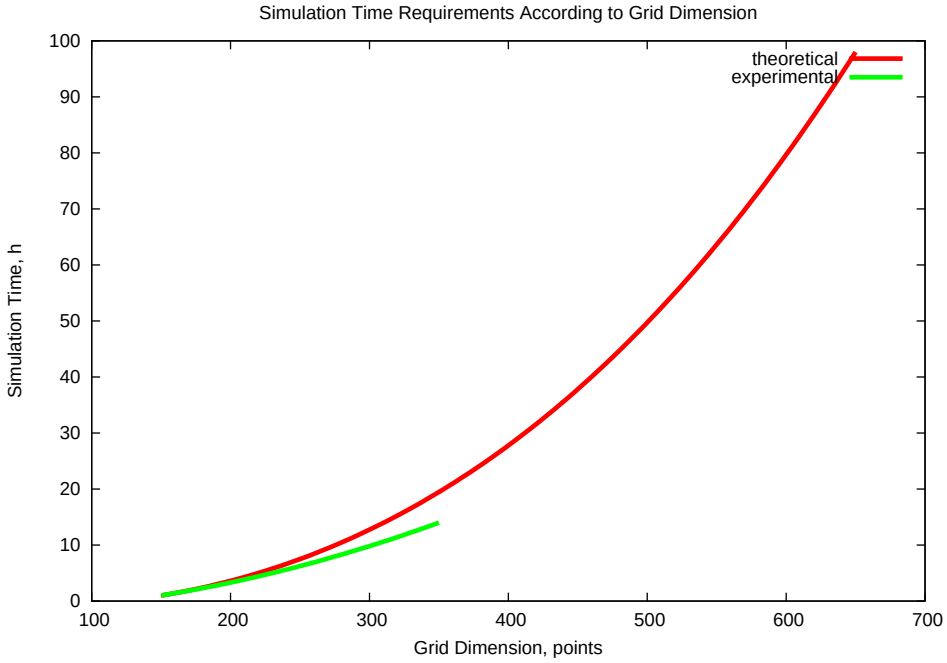

Figure 2.5: Simulation Time Requirements According to Grid Dimension

Every compute node is comprised by the 32-bit dual core 700 MHz Power PC 440. It has a customised Floating Point Unit (FPU) called "Double Hammer" and 512 MB of RAM. The node runs a proprietary single-threaded micro operating system.

The I/O machines have the identical hardware configuration to the compute nodes. The only difference is that these systems are governed by the Linux OS with a communication daemon. One I/O machine is responsible for the I/O operations of 8 compute nodes. Aimed for high speed and large volume I/O operations these systems are also equipped with 1 Gb ethernet connection. Figure 2.6 represents the overall IBM BlueGene/L architecture. The compute card on this scheme is a single compute node described previously.

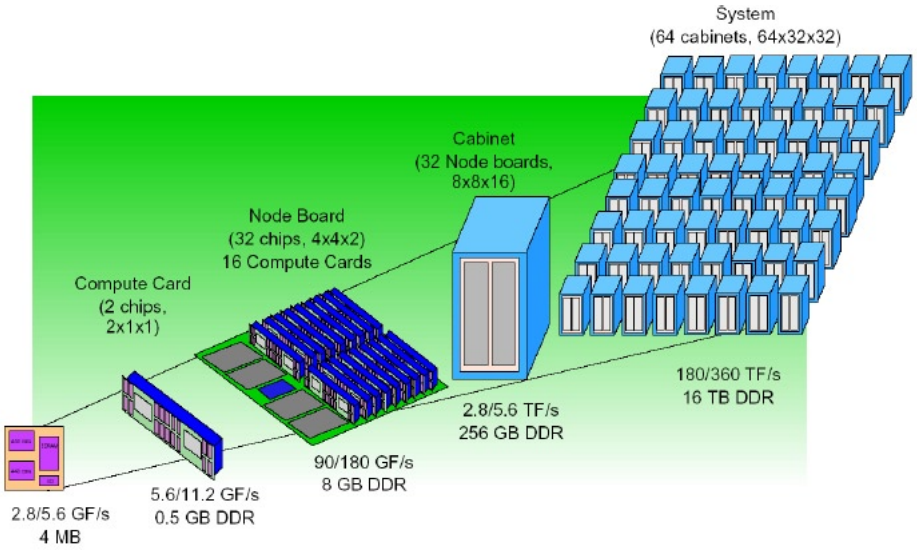

Figure 2.6: IBM BlueGene/L System Overview

2.2.2 Drawbacks

The Astron/Lofar BGL system has some known drawbacks. First of all, there are 8 times less I/O nodes than computing nodes, since one I/O node is responsible for input and output of 8 computing nodes. Hence I/O intensive computation can easily damage the whole system.

Secondly, each node has only 0.5 GB of memory. Since the current code developed in Manchester was designed to work with 2 GB of memory per node, it is necessary to modify this code to run successfully on 512 MB of RAM in the IBM BlueGene/L in Astron. Despite of these problems as well as minor configuration errors of the resource management system, the BGL offers an enormous amount of computing power. This makes it a unique high performance system with invaluable potential for our FD-FDTD simulations.

2.2.3 Current Experience

First of all the original FD-FDTD code has been tailored to make it work on the Astron/Lofar machine in the Netherlands. The code in Manchester was successfully compiled using the IBM Fortran 95 compilers. Simple test simulations were also run on the BGL. Unfortunately, due to the mis-configuration of the resource management system, only up to 32 computing nodes were used. Configuration errors are being currently fixed.

2.2.4 Potential Performance

Based on the experimental data obtained from Horace (see 2.1.3) it is possible to estimate the maximum number of antenna elements and cubic grid space dimension that could be efficiently simulated on the Astron/Lofar BlueGene/L machine. The maximum amount of processors that could be requested on the BGL for one job is 1024. Each node on BlueGene/L has 512 MB of operating memory. Therefore, the total amount of RAM available for simulation will be 512 GB. Now dividing the total RAM by the RAM required for simulation of one antenna element will give the potential maximum of antenna elements that could be calculated on the BGL system: $512 \text{ GB} \,/\, 1.768 \text{ GB} \approx 289$ antennas. The maximum size of the cubic space grid equals to $\sqrt[3]{\frac{512 \text{ GB}}{1.06 \times 10^{-7} \text{ GB}}} \approx 1690$ points.

2.3 Hierarchical Data Format (HDF5)

2.3.1 Format Overview

The calculations in the previous section show that storing simulation data in ASCII form is not efficient. There are alternative file formats developed specifically for scientific data storage. Among these are HDF5, HDF4, NetCDF, PDB and FITS. The HDF5 file format was chosen.

Justification of the choice is as follows:

Some of HDF5 properties are similar to those offered by alternative formats, but there are many spheres where HDF5 is more flexible and beneficial in comparison to its rivals.

HDF5 does not set any limit on the data file size and the number of objects stored in a single file. There are many programming interfaces developed to enable HDF5 functionality on wide variety of computing platforms. These include C, C++, Java and Fortran 90 interfaces. The format has a versatile data model making it possible to express other formats in terms of HDF5.

HDF5 offers wide means for describing the data with common and user-defined metadata. The Virtual File Layer (VFL) abstraction enables efficient I/O operations, including standard, parallel and network I/O. HDF5 parallel data processing mechanism relies on MPI I/O, specified by the MPI-2 standard. The HDF5 I/O library is dual-layered and might be used differently. On the high-level of abstraction it offers object-specific and on

the low-level media-specific APIs. It also supports diverse storage media. HDF5 split driver stores data in two physical files – one for meta- and the other for raw data.

Many strategies exist to optimise efficient storage and manipulation of data. The data could be compressed and chunked, and data structures extended and updated. HDF5 compresses data in GNU zlib by default, but it could be replaced by any other compression algorithm. Chunking strategy proves to be very efficient, especially in cases when partial data access is needed.

In general, HDF5 provides the highest degree of collaboration among all of its competitors. System-independent file format makes HDF5 datasets highly portable. These files could be accessed from machines with different memory and storage architectures. HDF5 is a perfect method for research data standardisation. Putting in place conventions on the way to organise and store data and metadata enables high data exchange, sharing and reuse. Having comparable performance level with all of its rivals HDF5 excels in a much broader feature support. This format's unique properties like optimised parallel processing, unlimited file size, chunking, compressing and complex datatype support are critical in the FDTD research. These capabilities of HDF5 grant enough freedom for finding the most effective solution for the current task of a Vivaldi antenna array simulation and will make a sound basis for the future work.

2.3.2 Output File Structure

The HDF5 operates with two general types of objects. Groups and datasets comprise the primary objects, and datatypes and dataspaces are the secondary or auxiliary objects. Figure 2.7 represents the HDF5 object hierarchy. The main entity of an HDF5 file is a dataset. This is the general container where the actual simulation data will be stored. The dataspace could be thought of as a coordinate system. Each point in the dataspace is represented by a 1-dimensional array, which may contain up to 6 electromagnetic field values. This means the datatype of the simulation dataset is a 1-dimensional array of length 9, which includes the Cartesian coordinates of a grid point. The chunking feature of HDF5 is also used to provide more efficient data access and more importantly better data compression. The dataset is shuffled and then compressed with the standard GNU zlib library algorithm.

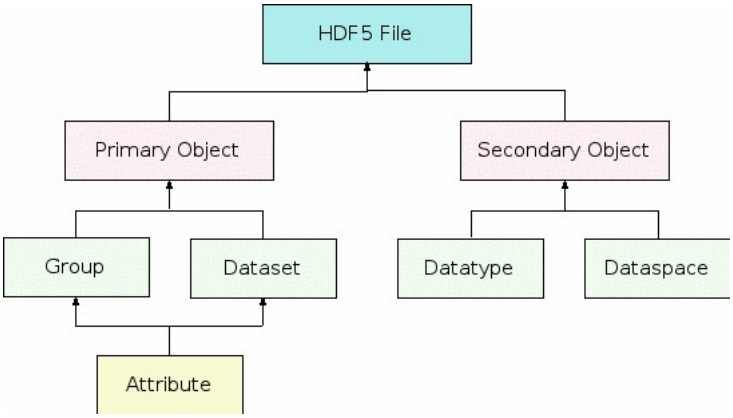

Figure 2.7: HDF5 Object Hierarchy

2.4 Conclusion

The world of high performance computing resides on the three whales: (i) available amount of CPUs and operating memory, (ii) efficiency of the I/O mechanism and (iii) the quality of the load balancing subsystem. The overall performance picture is complicated by the interdependencies which exist between the I/O efficiency and the amount of RAM and also the I/O efficiency and the load balancing subsystem.

Finite Difference Time Domain (FDTD) is very CPU and RAM demanding and also puts high emphasis on the I/O mechanism. The solution to this is a trade-off between the simulation's performance, speed and precision. Some of these components have to be compromised in order to produce reasonable simulation results.

One of the current research topics is the reduction of the I/O workload. It is planned to introduce different data storage and output patterns that would potentially improve the overall program's performance and implement the HDF5 data format for storing the output. Another innovation will be the clever output approach, which will print out only the existing electromagnetic field values. This means the time will be saved on all zero field values.

There are many aspects of the work that require further investigation such as the study on whether or not the program output time depends on the file size and format. This could be done by performing simulations with the gradual increase of output, e.g. simulation without any output, with one field value only E_z, and with six field values H_x, H_y, H_z, E_x, E_y and E_z.

The impact of HDF5 usage on overall storage space demand is another issue which needs experimental support. It is obvious that application of HDF5 will be beneficial, but the degree and character of this benefit should be tested in greater detail.

Chapter 3

Characteristic Impedance of the Rectangular Coaxial Cable

For the system development of a Vivaldi antenna array, characteristic impedance is required. The method to calculate the characteristic impedance out of FDTD simulation results is first investigated.

3.1 Characteristic Impedance Calculation and Analysis

The E_y and H_x electromagnetic field values were used for the characteristic impedance calculation of a rectangular coaxial wire. The ratio of peak magnitude of these two field values is the cable's impedance. These values were taken at the dielectric area of the cable. The geometry of the simulated rectangular cable is shown in Figure 3.1.

The soft source is used for the excitation of the FDTD space. The excitation location area is constituted by: x=43-57 cells, y=99 cell and z=43-57 cells. Hence, it is an area just outside of the cable geometry (see Figure 3.1) which is covering the whole of the first dielectric part, then the metal core and the second dielectric part. The excitation waveform is a modulated Gaussian pulse.

The electric and magnetic fields were observed just outside, at the surface and just inside of the cable. The most useful values was just inside the dielectric of the cable. The electromagnetic wave propagates only inside the dielectric at every type of wire, waveguide and planar transmission line. The exact point of the FDTD grid which was used in the impedance calculation is: $x = 45$, $y = 102$, $z = 50$. The characteristic impedance of the rectangular coaxial cable was calculated at the above values of the FDTD space. It was computed from the ratio of the electric field at the y-axis over the magnetic field at the x-axis. These fields were simulated with the FDTD method. The peak values in amplitude were used for the calculation of the impedance

The ratio of the calculated electric and magnetic field values is the impedance of the square coaxial line. It is given by the following:

$$Z = \frac{E_y}{H_x} = 27.53\Omega \tag{3.1}$$

Furthermore, at the middle of the cable's dielectric and at the excitation point ($x = 45, y = 99, z = 50$), the impedance was computed to be: $Z = 28.92\Omega$. A good agreement is obtained between the calculated impedance from the FDTD and the impedance of the same simulation with the software CST Microwave Studio. The characteristic impedance from the commercial software was: $Z = 28.73\Omega$. Furthermore, there is an excellent agreement with the analytical formula that is computing the impedance of a square coaxial line. The analytical impedance value is $Z = 30.84\Omega$. All the previous comments can be observed in the Figure 3.2.

At the cable's edges, where the wire's dielectric is finished and the metal shield is beginning, the coordinates of the FDTD mesh through the x-axis are $x = 43$ and $x = 47$ and the y, z axis have variable values. From the Figures 3.3 and 3.4, at these points the impedance can be calculated just outside of the cable ($y = 97$), in free space.

At the point $x = 44$, the value of the characteristic impedance can be calculated, with a good agreement to the CST Microwave studio, between $y = 101$ and $y = 102$ points of the FDTD mesh space. This behaviour is depicted in Figure 3.5. At $x = 46$ point, the electromagnetic field is more affected by the inner metal cable part which is shown in Figure 3.6.

From Figure 3.3– Figure 3.6, it can be observed that all the plotted curves have similar behaviour. Especially, the $y = 100$ point of the FDTD grid is where the free space is changing to the cable geometry. Consequently, this is a place of discontinuity between vacuum space and dielectric or metal FDTD mesh. At this particular point, the boundary conditions will seriously affect the electromagnetic field values and the field distribution in general. The effect of this discontinuity can be observed from the impedance plots. Particularly, all the graphs have a minimum impedance value at the $y = 100$ point. Furthermore, at the most problematic place of calculation ($x = 47$), the value of impedance at the boundary point ($y = 100$) is almost equal to zero. It is obvious from the FDTD simulation that this boundary condition point is strongly distorting the correct cable impedance calculation. As a result, this point is definitely not appropriate for every kind of electromagnetic computations. Moreover, when the point $y > 103$ and the electromagnetic wave is propagating deep inside the dielectric material, the impedance calculation is affected. From the figures, it is observed that for all the possible x positions deep inside the dielectric, the impedance is extremely high. Hence, it is not an appropriate place for electromagnetic calculations due to the reflections of the inner and outer cable's metallic areas. Another point, where it is not possible to calculate the impedance, is when $y < 97$. At this point, the electromagnetic wave is totally dispersed in space after coming out from the cable's feeding point. The values of the impedance that are calculated to these areas are smaller than the expected ones due to the wave dispersion. However, there are not equal to the free space wave impedance ($Z_o = 120\pi\Omega = 377\Omega$) because these points are close to the cable's edges and the electromagnetic field pattern is seriously affected by the field distribution inside the dielectric of the wire.

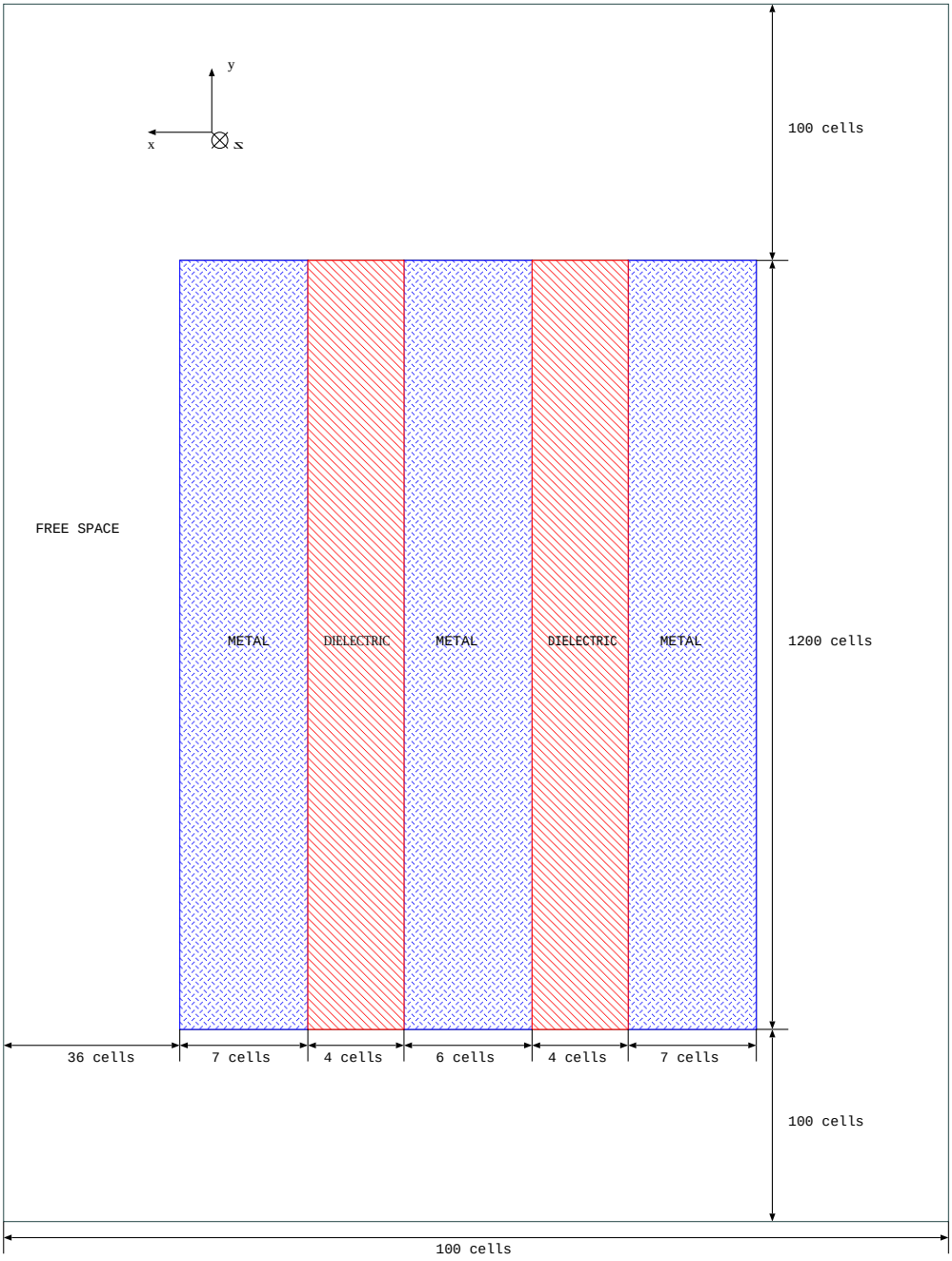

Figure 3.1: Geometry of the Rectangular Cable

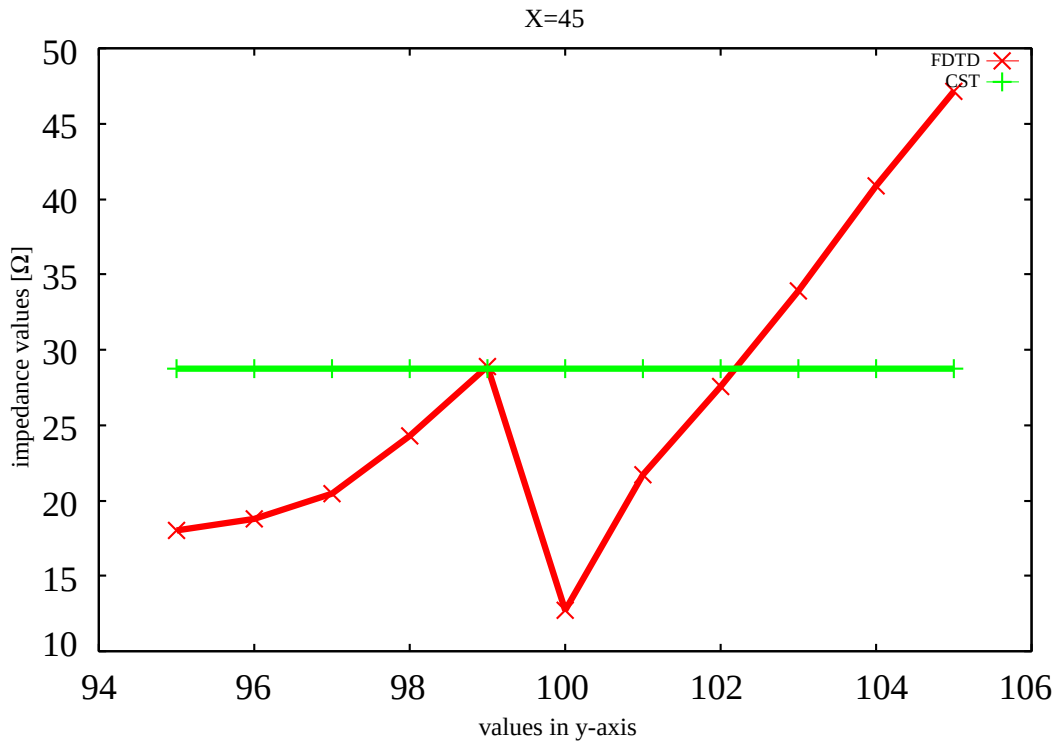

Figure 3.2: FDTD and CST Calculation of Cable Impedance at $x = 45$

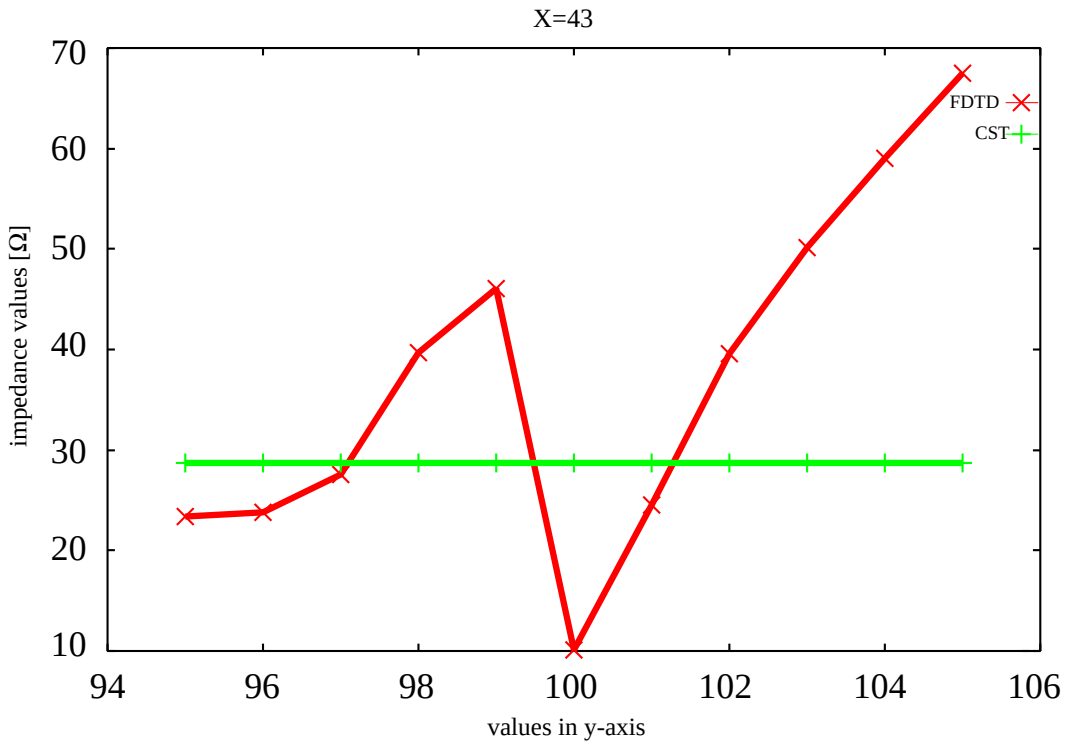

Figure 3.3: FDTD and CST Calculation of Cable Impedance at $x = 43$

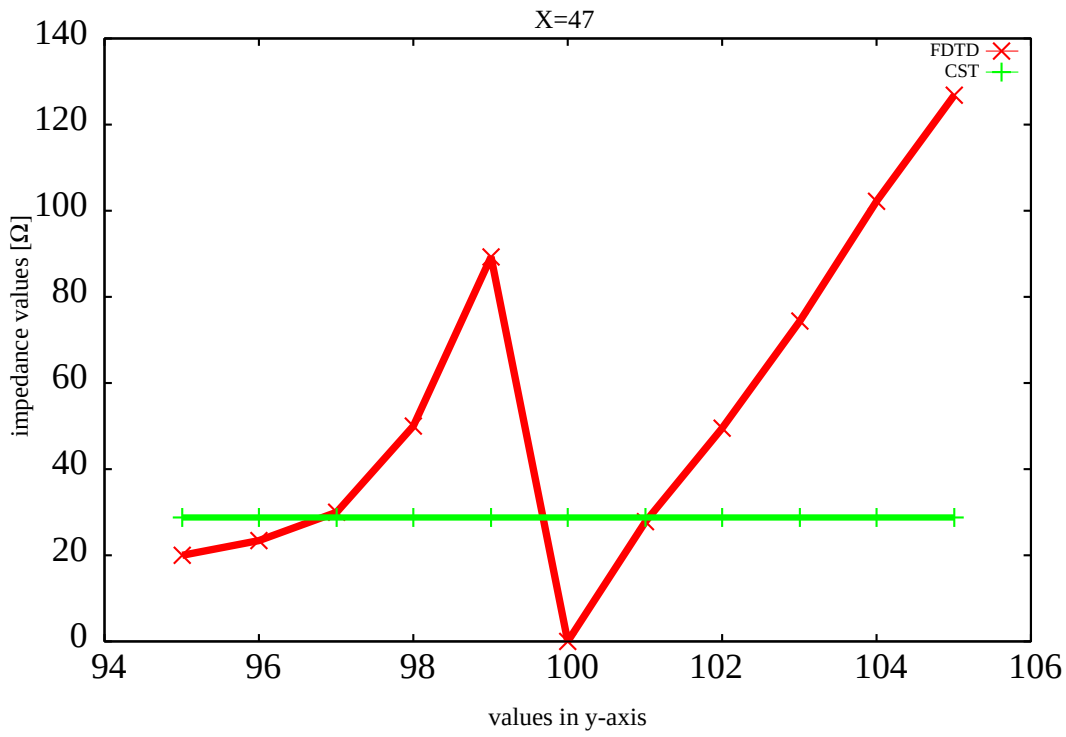

Figure 3.4: FDTD and CST Calculation of Cable Impedance at $x = 47$

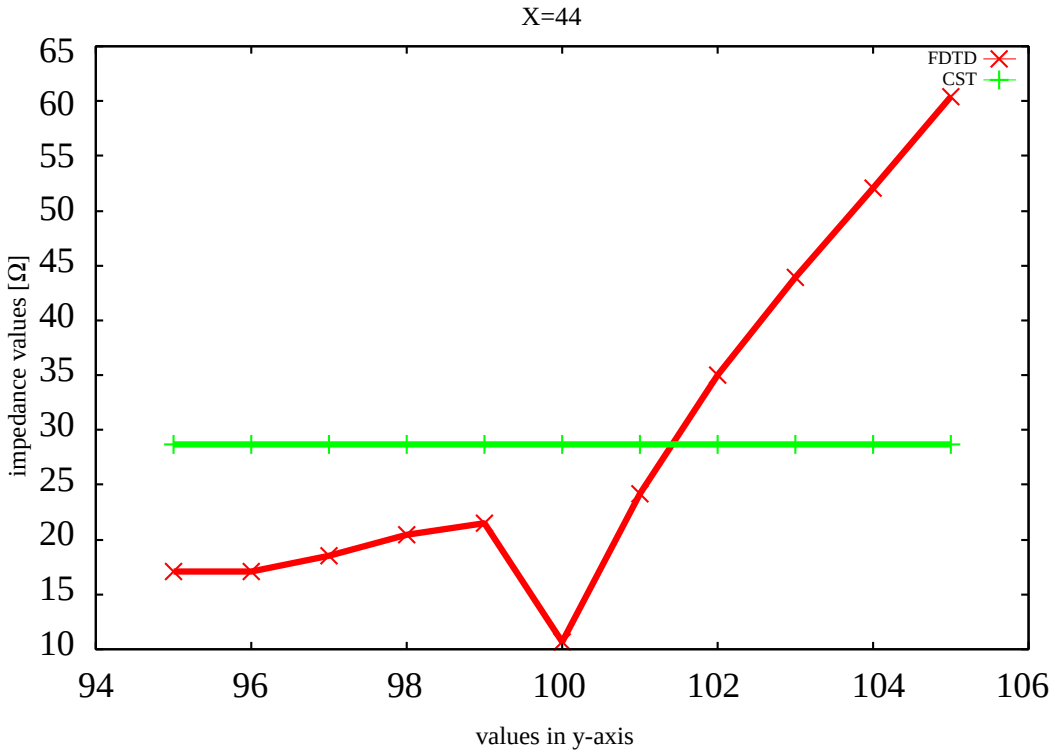

Figure 3.5: FDTD and CST Calculation of Cable Impedance at $x = 44$

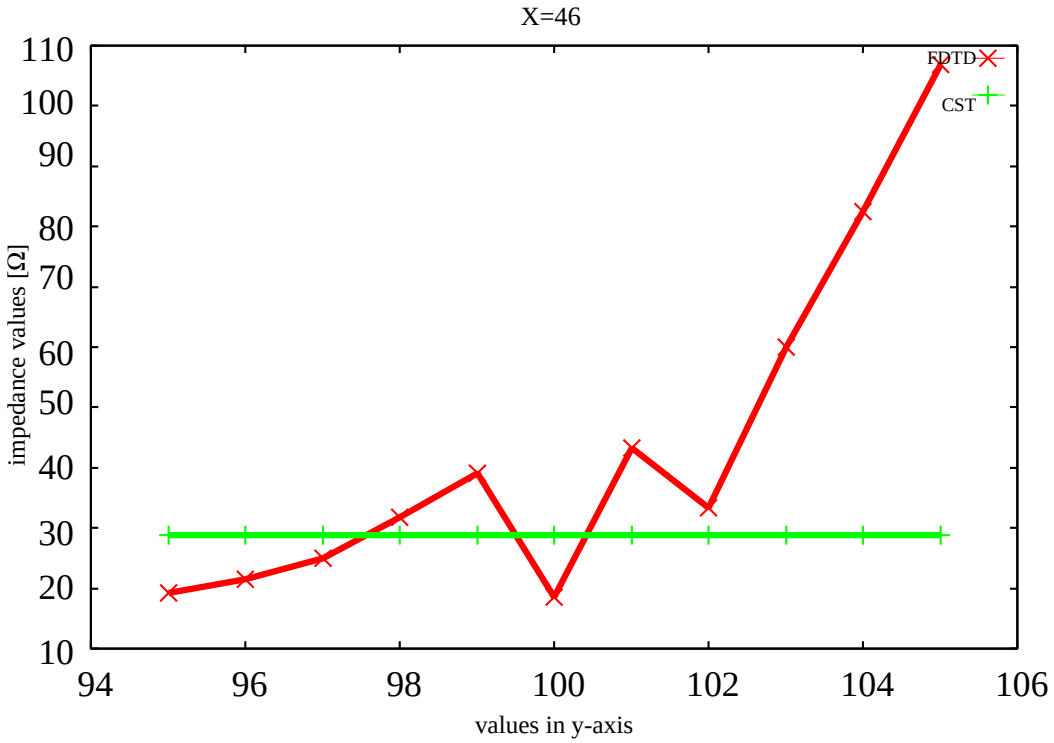

Figure 3.6: FDTD and CST Calculation of Cable Impedance at $x = 46$